A dTDP-L-Rhamnose 4-epimerase required for glycopeptidolipid biosynthesis in Mycobacterium abscessus

John Jairo Aguilera-Correa, Fangyu Wei, Louis-David Leclercq, Yara Tasrini, Edukondalu Mullapudi, Wassim Daher, Kazuki Nakajima, Stéphane Canaan, Jean-Louis Herrmann, Matthias Wilmanns, et al.

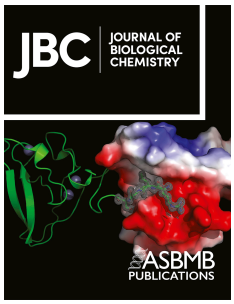

A dTDP-L-Rhamnose 4-epimerase required for glycopeptidolipid biosynthesis in *Mycobacterium abscessus*

John Jairo Aguilera-Correa, Fangyu Wei, Louis-David Leclercq, Yara Tasrini, Edukondalu Mullapudi, Wassim Daher, Kazuki Nakajima, Stéphane Canaan, Jean-Louis Herrmann, Matthias Wilmanns, Yann Guérardel, Liuqing Wen, Laurent Kremer

PII: S0021-9258(24)02354-8

DOI: https://doi.org/10.1016/j.jbc.2024.107852

Reference: JBC 107852

To appear in: *Journal of Biological Chemistry*

Received Date: 12 July 2024

Revised Date: 11 September 2024

Please cite this article as: Aguilera-Correa JJ, Wei F, Leclercq LD, Tasrini Y, Mullapudi E, Daher W, Nakajima K, Canaan S, Herrmann JL, Wilmanns M, Guérardel Y, Wen L, Kremer L, A dTDP-L-Rhamnose 4-epimerase required for glycopeptidolipid biosynthesis in *Mycobacterium abscessus*, *Journal of Biological Chemistry* (2024), doi: https://doi.org/10.1016/j.jbc.2024.107852.

A dTDP-L-Rhamnose 4-epimerase required for glycopeptidolipid biosynthesis in *Mycobacterium abscessus*

John Jairo Aguilera-Correa[1], Fangyu Wei[3,$], Louis-David Leclercq[4,5,$], Yara Tasrini[1,$], Edukondalu Mullapudi[6], Wassim Daher[1,2], Kazuki Nakajima[7], Stéphane Canaan[8], Jean-Louis Herrmann[5], Matthias Wilmanns[6,9], Yann Guérardel[4,7], Liuqing Wen[3], and Laurent Kremer[1,2*]

[1]Centre National de la Recherche Scientifique UMR 9004, Institut de Recherche en Infectiologie de Montpellier (IRIM), Université de Montpellier, 1919 route de Mende, 34293, Montpellier, France.
[2]INSERM, IRIM, 34293 Montpellier, France.
[3]Shanghai Institute of Materia Medica, Chinese Academy of Sciences, Chinese Academy of Sciences, 555 Zuchongzhi Rd, 201203, Shangai, China
[4]Univ. Lille, CNRS, UMR 8576 - UGSF - Unité de Glycobiologie Structurale et Fonctionnelle, F-59000 Lille, France.
[5]Université Paris-Saclay, UVSQ, Inserm, Infection et inflammation, 78180, Montigny-Le-Bretonneux, France.
[6]European Molecular Biology Laboratory, Hamburg Unit, Notkestrasse 85, 22607 Hamburg, Germany.
[7]Institute for Glyco-core Research (iGCORE), Gifu University, Gifu, Japan
[8]Aix-Marseille Univ, CNRS, LISM, IMM FR3479, Marseille, France.
[9]University Medical Center Hamburg-Eppendorf, Martinistrasse 52, 20246 Hamburg, Germany.

[$]Equal contribution

*Corresponding author: Laurent Kremer; Tel: (+33) 4 34 35 94 47; E-mail: laurent.kremer@irim.cnrs.fr

Running title: Tle epimerase is required for glycopeptidolipid synthesis

Keywords: *Mycobacterium abscessus*, cell wall, glycopeptidolipid, Rhamnose, 6-deoxy-Talose, epimerase, morphotype, virulence, zebrafish.

ABSTRACT

Mycobacterium abscessus causes severe lung infections in cystic fibrosis patients and exhibits smooth (S) or rough (R) morphotypes. Disruption of glycopeptidolipid (GPL) production results in the S-to-R transition but the underlying molecular mechanisms of this transition remain incompletely understood. Herein, we characterized MAB_4111c in relation to GPL synthesis and investigated the effects of *MAB_4111c* deletion in *M. abscessus* pathogenicity. An enzymatic assay indicated that MAB_4111c, also designated Tle for Talose epimerase, is converting dTDP-L-Rhamnose into dTDP-6-deoxy-L-Talose. A *tle* deletion mutant was constructed in the S variant of *M. abscessus* and relative areas of Rhamnose and 6-deoxy-Talose and their methylated forms expressed as ratios of total monosaccharides, showed an altered GPL profile lacking 6-deoxy-Talose. Thus, Tle provides dTDP-6-deoxy-L-Talose, subsequently used by the glycosyltransferase Gtf1 to transfer 6-deoxy-Talose to the GPL backbone. Strikingly, the *tle* mutant exhibited a R morphotype, showed impaired sliding motility and biofilm formation, and these phenotypes were rescued upon functional complementation. Moreover, deletion of *tle* in *M. abscessus* results in increased pathogenicity and killing in zebrafish embryos. Together, our results underscore the importance of the dTDP-L-Rhamnose 4-epimerase activity in GPL biosynthesis and in influencing *M. abscessus* virulence.

INTRODUCTION

M. abscessus is an emerging opportunistic pathogen causing a variety of human infections that usually involve the skin and subjacent soft tissues, but also severe lung infections in patients with various chronic lung disorders, such as bronchiectasis and chronic obstructive pulmonary disease or cystic fibrosis (1, 2). This mycobacterium is intrinsically resistant to β-lactams, tetracyclines, aminoglycosides, and macrolides, which are routinely used to treat Gram-negative and Gram-positive bacterial infections (3), rendering treatments extremely challenging (4). Like other non-tuberculous mycobacteria (NTMs), *M. abscessus* has shown the ability to develop biofilms, structured bacterial aggregates enclosed in a self-produced polymeric matrix where multiple and complex socio-microbiological relationships reign, in the environment, water distribution systems (5, 6), hospital equipment (5, 6), human tissues, e.g., lungs (7), and medical devices (8, 9). This rapidly-growing mycobacterium can be found as smooth (S) or rough (R) variants and these morphotypes rely mainly on the production of high (in S) or low (in R) levels of glycopeptidolipids (GPLs), respectively (10–12). Genome sequencing identified multiple indels in the *gpl* locus of the R strain as compared to the S strain (13) mainly in *mps1* and *mps2,* encoding non-ribosomal peptide synthases responsible for the biosynthesis of the GPL peptide backbone, and in *mmpL4a*/*mmpL4b,* encoding membrane proteins involved in GPL transport (13–15). Thus, these genetic changes in the *gpl* locus result in the irreversible loss of the GPL and are directly responsible for the R colony morphology (13).

GPLs are found in the outer leaflet of numerous NTMs (16). These lipids are pivotal for aggregation, biofilm development, motility, interaction with host cells and pathogenesis (16–22). Both S and R forms are isolated from sputums of patients with chronic lung infections but while the S form is thought to represent the environmental variant of *M. abscessus* (which infects and colonizes the lungs), the R form emerges from the S form within the infected host (18, 23, 24). Several studies support the enhanced pathogenesis of the R form over the S form, the former being associated with more persisting and aggressive infections in addition to the decline of the lung functions (18, 25–28). In the context of infection with *M. abscessus*, the zebrafish model has deserved considerable interest as it was used to help defining the interactions between *M. abscessus* and the innate immune response (27, 29). In particular, zebrafish embryos are killed by the *M. abscessus* R infection, as evidenced by intense bacterial proliferation, production of serpentine cords, abscesses and inflammation (27, 30). These features are in agreement with

epidemiological surveys, which support the prominence of the R variant in patients with severe lung infections and chronic airway colonization in cystic fibrosis patients (18, 24). Overall, this highlights the clinical relevance of morphological distinctions between S and R morphotypes and importance to understand the S-to-R transition at a molecular level (13).

The general GPL structure consists of a mixture of 3-hydroxy and 3-methoxy C28-30 fatty acids amidated by a tripeptide-amino-alcohol (D-Phe-D-*allo*-Thr-D-Ala-L-alaninol) (10). This lipopeptide core is glycosylated on the *allo*-Thr linked with a 6-deoxy-α-L-Talose (6-d-Tal) and on the alaninol linked with an α-L-Rhamnose (Rha) (10). Some GPLs can be di-glycosylated containing a 3,4-di-*O*-acetylated 6-d-Tal and a 3,4-di-*O*-methylated or 2,3,4-tri-*O*-methylated Rha (31–34). We previously demonstrated that the glycosyltransferases Gtf1, Gtf2 and Gtf3, encoded within the *gpl* locus, transfer the 6-d-Tal, the first Rha and the second Rha to the lipopeptide core, respectively (35). Importantly, in a *gtf1* deletion mutant, the synthesis of GPL derivatives lacking 6-d-Tal leads to a R morphotype, mycobacterial cording and increased virulence and pathogenicity in zebrafish (35). This illustrates the importance of Gtf1 in modelling the GPL structure and in influencing *M*. *abscessus* virulence, although the functional and structural characterization of this enzyme remains to be established. In addition, the enzyme/pathway that provides dTDP-6-d-Tal, the substrate used by Gtf1 to talosylate GPL, remains unknown.

In mycobacteria, L-Rha is synthesized *via* the essential Rml pathway that generates dTDP-L-Rha from Glc-1-phosphate (36). This pathway is composed of four enzymes - RmlA (MAB_4113), RmlB (MAB_3779), RmlC (MAB_3780), and RmlD (MAB_3613c) - encoded by four genes that are not in close vicinity in the *M. abscessus* genome, except for *rmlB* and *rmlC*. Besides being a component of GPLs, Rha can be found in other glycolipids, such as phenolic glycolipids (37) and is present in all mycobacteria as being part of the linker disaccharide (Rha-N-acetyl-glucosaminyl-phosphate) unit that attaches the cell wall arabinogalactan (AG) to the peptidoglycan (PG) layer (36). In contrast to Rha, 6-d-Tal is an infrequent deoxyhexose found only in bacteria, essentially in the cell wall and capsules (38). The dTDP-6-d-Tal is the activated form of 6-d-Tal and it is synthesized from Glc-1-phosphate and dTTP partially or entirely *via* the Rml pathway. In *Haemophilus actinomycetemcomitans* NCTC9710 serotype C (partial synthesis *via* the Rml pathway), the first three enzymes, RmlA-C, are identical to those required to synthesize dTDP-L-Rha. The fourth enzyme, a dTDP-6-deoxy-L-talose 4-dehydrogenase (Tll) is also a dTDP-4-keto-6-deoxy-L-mannose reductase such as RmlD, but the stereoselectivity of Tll regulates dTDP-4-keto-6-deoxy-L-mannose, which is reduced to dTDP-6-deoxy-L-Talose (39). In *Burkholderia*

114 *thailandensis* (complete synthesis *via* the Rml pathway), a dTDP-L-Rha 4-epimerase, WbiB,
115 converts dTDP-L-Rha into dTDP-6-d-Tal (40). Interestingly, in *M. abscessus*, a paralogous *rmlB*
116 gene (*MAB_4111c*) is present in the *gpl* locus (31) and *in silico* predictions suggest that
117 *MAB_4111c* encodes a putative epimerase/dehydratase (41).

118 Herein, we focused on MAB_4111c to further advance our understanding of the synthesis of
119 the dTDP-6-d-Tal substrate of Gtf1 and the presence of 6-d-Tal in the GPL of *M. abscessus.* We
120 also aimed to study the consequences of *MAB_4111c* deletion on bacteriological features and
121 disease pathology in this emerging pathogen in zebrafish. Bioinformatic and genetic studies were
122 also performed to determine the distribution and prevalence of *MAB_4111c* orthologous genes
123 in other NTMs.

RESULTS

MAB_4111c encodes a preditive dTDP-L-Rhamnose 4-epimerase

The S variant of *M. abscessus* synthesizes both diglycosylated GPL (GPL-2a) and triglycosylated GPL (GPL-3), containing one and two partially *O*-methylated Rha residues, respectively, as well as a di-*O*-acetyl 6-d-Tal residue **(Figure 1A).** While most proteins encoded by the *gpl* cluster and involved in the biosynthesis and transport of GPL have been characterized to date, the enzyme catalyzing the interconversion between dTDP-Rha and dTDP-6-d-Tal in mycobacteria remains enigmatic. *MAB_4111c* is located between *gtf3*, encoding the rhamnosyltransferase which adds the second Rha to generate GPL-3 (35), and *atf2*, encoding an acetyltransferase which acetylates the 6-d-Tal (34) **(Figure 1B)**. Bioinformatics analysis suggests that MAB_4111c may code for an enzyme with epimerase activity, in agreement with a BLAST analysis which showed that MAB_4111c shares 54% identity with WbiB, a dTDP-Rha 4-epimerase in *Burkholderia thailandensis*, the first enzyme reported to catalyze the interconversion between dTDP-Rha and dTDP-6-d-Tal (40). This analysis also shows that the putative catalytic Tyr residue (Y181) as well as other residues participating in the binding of the NADH cofactor and dTDP-Rha substrate are fully conserved in MAB_4111c **(Figure 1C).**

MAB_4111c converts dTDP-Rhamnose into dTDP-6-deoxy-Talose

To experimentally validate the function of MAB_4111c as a dTDP-Rha 4-epimerase, a His-tagged version of the protein was produced in *Escherichia coli.* Initial attempts to express and purify soluble MAB_4111c for biochemcial and structural analyses yielded insufficient protein quantities. Thus, we generated a MAB_4111c-enriched soluble fraction obtained after partial purification on Ni^{2+}-coated beads, which was assayed by incubation with $NADP^+$ and dTDP-Rha and monitored for the production of dTDP-6-d-Tal **(Figure 2A)**. The HPLC profile shows the presence of a weak signal with a retention time (RT) similar to the one of the dTDP-6-d-Tal standard (**Figure 2B, upper panel)**. The nature of the observed weak signal was assessed by LC/MS analysis in multiple reaction monitoring (MRM) mode **(Figure 2C)**. As shown in the upper panel, the use of specific precursor ion $[M-H]^-$ at *m/z* 547.1, characterisitic of dTDP-dHex, showed two signals with RT similar to dTDP-Rha and dTDP-6-d-Tal. Fragmentation of the minor signal produced a MS/MS spectrum identical to standard dTDP-6-d-Tal, demonstrating that the minor signal corresponds to dTDP-6-d-Tal **(Figure 2C, lower panel)**. Finally, NMR analysis of the total

reaction mixture showed signals characteristic of dTDP-6-dTal, along with signals attributed to the substrate dTDP-Rha, further demonstrating that MAB_4111c transforms dTDP-Rha into dTDP-6-d-Tal **(Figure 2D)**. Specifically, weak proton signals at 5.17, 4.05, 3.82, and 3.75 ppm are characteristic signals of dTDP-6-d-Tal. According to the NMR spectrum of the dTDP-6-d-Tal standard, proton signals were elucidated as H1 (δ5.17 ppm), H2 (δ4.05 ppm), H3 (δ3.82 ppm) and H5 (δ3.75 ppm) of 6-d-Tal. The signal of H-4 proton (δ3.65 ppm) in 6-d-Tal is overlapped with H-4 proton signal of Rha. Kinetic analysis indicated that MAB_4111c could convert dTDP-Rha into dTDP-6-d-Tal with a 3-4% conversion rate within an hour, reaching a 7% conversion rate after 300 min of incubation **(Figure 2E)**. To address the specificity of the reaction, a similar assay was set up by replacing dTDP-Rha by dTDP-Glc in the reaction mixture, where no dTDP-6-d-Tal was detected **(Figure 2B, lower panel)**. In addition, we also assayed the reverse reaction using dTDP-6-d-Tal as a substrate and observed the formation of dTDP-Rha after 60 min of reaction (data not shown), thus confirming that MAB_4111c catalyzes both reactions.

Overall, these results suggest that MAB_4111c is an epimerase that specifically converts dTDP-Rha into dTDP-6-d-Tal *in vitro*. Given its activity, we propose to rename the protein Tle for Talose epimerase, based on a previous nomenclature used to designate a similar enzyme in *Acinetobacter baumannii* (42).

Structural prediction of Tle

Since we could not produce high yields of Tle for structural analysis, we employed AlphaFold 3 for structural predictions (43). We first screened the Protein Data Bank (PDB) for experimentally determined epimerase structures, most of which are dimeric. Sequence identity between Tle and available epimerase structures ranged from approximately 23-32%. Despite low sequence identity, epimerases typically exhibit high structural homology. Using AlphaFold 3, we generated a dimeric structure of Tle in the presence of NAD^+. The prediction covered more than 90% of the structure with a very high predicted local distance difference test (pLDDT) score **(Figure 3A)**. The oligomeric state prediction yielded predicted template modelling (pTM) and interface predicted template modelling (ipTM) values of 0.91 and 0.92, respectively, indicating that the predicted structure can be used with confidence for further analysis. The structure reveals a classic Short-Chain Dehydrogenase/Reductase (SDR) fold (44) **(Figure 3B)**. The dimeric interface is formed by two α-helices from each protomer (residues 88-110 and 180-199), creating a four-α-helix bundle **(Figure 3B)**. The overall architecture includes an N-terminal NAD^+ binding domain, a typical

Rosmann fold and a C-terminal substrate-binding domain **(Figure 3B)**. Comparison of the AlphaFold-generated Tle structure with the known *Pseudomonas aeruginosa* UDP-N-acetylglucosamine 4-epimerase WbpP (PDB code:1SB8) epimerase structure yielded a root mean square deviation (RMSD) of approximately 1.37 Å **(Figure 3B)**, suggesting a high degree of structural similarity. WbpP was used because it had one of the best RMSD scores in our analysis. Notably, Tle includes an extended secondary structure element from residues 128 to 165, characterized by an additional α-helix, long loop and a pair of antiparallel β-strands. This feature contrasts with WbpP, which has a shorter loop in the corresponding region, highlighting a distinctive structural variation in Tle **(Figure 3B)**.

We next compared the AlphaFold-predicted structure of Tle with the known WbpP structure to identify the key residues involved in catalysis. The binding site for NAD^+, is highly conserved among SDR family enzymes (44). Structural alignment with WbpP confirmed that majority of the NAD^+ binding residues are conserved in Tle **(Figure S1A)**. However, some differences were noted: V30, H32, and H36 in Tle correspond to N48, A50, and G52 in WbpP **(Figure S1B)**. The catalytic triad, which is typically represented as SYK in the SDR family (44–46) is conserved in Tle as S121, Y181, and K185 **(Figure S1B)**. No activity was observed when replacing the wild-type enzyme by the Tle-Y181A mutant in the assay **(Figure 2B and 2D)**, thus indicating that introducing a Y181A change leads to a catalytically inactive enzyme. We also assessed the activity of Tle mutated proteins in which the conserved residues S121, N210, R249 **(Figure 1C and S1B)** were substitued by alanines. As for the His-tagged wild-type protein, the different mutated variants were enriched by affinity chromatography on Ni^{2+} beads and the amount of each protein visualized by Western blotting using anti-His antibodies **(Figure S2A).** The relative concentration of each protein was determined by comparing the grayscale of the bands using ImageJ and adjusted so that the same quantity of each protein was added to the assay in the presence of $NADP^+$ and dTDP-6-d-Tal. **Figure S2B** shows that none of these mutated proteins catalysed the formation of dTDP-6-d-Tal, confirming the importance of S121, N210, and R249 in the activity of Tle.

Overall, these data validate the AlphaFold model and supports the structural similarity between WbpP and Tle.

Bacteriological characterization of a *tle* deletion mutant in *M. abscessus*

To investigate the contribution and biological functions of the dTDP-L-Rha 4-epimerase in *M. abscessus*, *tle* was deleted in the GPL-producing S variant of *M. abscessus,* using a unmarked

deletion method (47) **(Figure S3A)**. PCR/sequencing performed on the parental and mutant strain (Δ*tle*) using the primers listed in **Table S1** confirmed the proper genotype of the mutant **(Figure S3B)**. Genetic complementation of the mutant was done through specific integration at the *attB* chromosomal site (48) of a copy of *tle* fused to a GFP-tag at the 3'-end and placed under the control of the endogenous promoter. Probing the crude lysates from the various strains using anti-GFP antibodies revealed a single band of the expected size, corresponding to the Tle-GFP fusion protein, validating complementation of the mutant **(Figure S3C)**.

A previous work had shown that deletion of *gtf1* in *M. abscessus* S was associated with R morphotype on agar plates (35). Observation of individual colonies showed that Δ*tle* formed R, corded colonies **(Figure 4A)**. Complementation of Δ*tle* (Δ*tle::*C), rescued the S morphotype **(Figure 4A)**. The growth of all strains in liquid culture describes a logistic growth (R^2>0.9 for all of them) **(Figure 4B and Table S4)**. The growth rate of Δ*tle* was higher than that of the R strain (p<0.0001), while the one of Δ*tle::*C was similar to the growth rate of the parental S strain. This indicates that deletion of *tle* slightly impacts on the replication rate of *M. abscessus* in planktonic culture. However, additional transmission electron microscopy observations failed to show significant changes regarding the size and ultrastructural organization of the cell wall in Δ*tle* **(Figure S4)**. Partitioning of mycobacterial pellets between hexadecane and aqueous buffer is used as a quantitative marker of cell surface hydrophobicity in mycobacteria to associate low pathogenicity with reduced hydrophobicity (49). To address whether deletion of *tle* affects surface hydrophobicity, aqueous hexadecane-buffer partitioning was applied to the S, R, Δ*tle*, and Δ*tle::*C strains. Δ*tle* appeared more hydrophobic than the parental S strain, in agreement with its R morphotype while the complemented strain displayed a hydrophobicity level similar to the parental S progenitor, correlating with its smoother morphological aspect **(Figure 4C)**. Consistent with the ability of the *M. abscessus* S variants to slide from the centre towards the periphery of the plates (11, 28), Δ*tle::*C, but neither R nor Δ*tle,* showed a higher sliding motility **(Figure 4D and 4E)**. Since sliding is dependent on the bacterial surface properties and interactions with the substrate, this suggests that Δ*tle* is likely defective in surface-associated cell wall components. The Δ*tle* colony biofilm was intermediate between the S and R biofilms **(Figure 4F)**, being broader and higher than the S biofilm **(Figure 4F, 4G and S5)**. In addition, the number of CFUs per membrane **(Figure 4H)**, the colony volume **(Figure 4I)** and density of the biofilm **(Figure 4J)** were very similar between the R and Δ*tle* strains. Δ*tle::C* showed no difference with the S progenitor.

We next investigated whether *tle* deletion affects drug susceptibility of *M. abscessus* towards a large panel of clinically used antibiotics. Δ*tle* showed only very slight changes in its antibiotype **(Table S5)**, for instance a slight increase against amikacin (MIC of 16 µg/mL for the wild-type strain and 32 µg/mL for Δ*tle*), tigecycline (MIC of 0.5 µg/mL for the wild-type strain to 1 µg/mL for Δ*tle*), and a slight reduction against imipenem (MIC of 64 µg/mL for the wild-type to 32 µg/mL for Δ*tle*), clarithromycin (MIC of 8 µg/mL for the wild-type strain and 4 µg/mL for Δ*tle*) or rifabutin (MIC of 64 µg/mL for the wild-type strain and 32 µg/mL for Δ*tle*).

Deletion of *tle* leads to the production of GPL lacking 6-d-Talose

We next evaluated the impact of *tle* deletion on the glycolipid content extracted from lyophilized mycobacteria. Analysis of the apolar lipid fraction by TLC shows that trehalose 6,6'-dimycolate (TDM) remains equally produced in all tested strains **(Figure 5A)**. Analysis of the polar lipid fractions indicates that, except in the R strain lacking GPLs (33, 35), GPLs are produced at high levels in all strains **(Figure 5A, left panel)**. However, while the parental S strain and Δ*tle::*C displayed an identical GPL profile, Δ*tle* exhibited lower migrating GPLs, resembling to those produced by Δ*gtf1* **(Figure 5A right panel and S6A),** a previously characterized mutant lacking the Gtf1 glycosyltransferase, which adds 6-d-Tal to the peptide backbone (35). Mild alkaline hydrolysis deacetylated polar lipids from S and Δ*tle::*C, as shown by the lower R_f of NaOH-treated compared to untreated ones GPL **(Figure 5B right panel)**. In contrast, saponification did not influence the GPL pattern of Δ*tle* and Δ*gtf1* **(Figure 5B right panel and S6C)**, suggesting that they are not acetylated, as previously demonstrated for Δ*gtf1* (35). Mass spectrometry analysis of native polar lipids from S and Δ*tle::*C showed ions at *m/z* 1258/1286 and 1404/1432 **(Figure 5C)**, previously identified as GPL-2a and GPL-3 **(Figure 1A)** (33, 34). After saponification, M-84 u.m.a ions at *m/z* 1173/1201 and 1319/1347 were detected, corresponding to dGPL-2a and dGPL-3, respectively, in agreement with the loss of the two acetyl groups substituting 6-d-Tal **(Figure 5C and S6C-D)**. MS spectra of native and saponified polar lipids isolated from Δ*tle* and Δ*gtf1,* all showed an intense ion at *m/z* 1187 accompanied with 1013/1041 pattern **(Figure 5C and S6C-D)**, previously attributed to the unnatural isomers GPL-2b and GPL-1b, which are devoid of 6-d-Tal (35). The absence of the 6-d-Tal was further confirmed by the monosaccharide composition analysis of the polar lipids, which demonstrates the lack of 6-d-Tal in Δ*tle* and Δ*gtf1* and its restoration in Δ*tle::*C **(Figure 5D and S6E)**.

Distribution of *tle* orthologs in NTMs and other bacteria

We identified and analyzed 107 proteins orthologus to Tle considering the inclusion and exclusion criteria described in the Materials and Methods. The neighbour-joining phylogenetic tree showed two clear clades related to mycobacterial genes and other bacterial species. Orthologous were found in at least 26 bacterial species belonging to the phyla Actinomycetota (genera *Nocardioides, Pseudonocardia, Desertimonas, Glaciibater, Curtobacterium,* and *Cryobacterium*) and Pseudomodota (genera *Burkholderia, Paraburkholderia, Xanthomonas, Rhizobium*, and *Chitinimonas*). Seventy-nine mycobacterial species, excluding *M. abscessus*, possess an orthologous gene to *tle* based on amino acid sequence analysis **(Figure 6A)**. These included 42 slowly-growing mycobacteria, one intermediately-growing mycobacterium and 36 rapidly-growing mycobacteria. This phylogenetic analysis indicates that Tle-related proteins can be found in bacteria but are over-represented in mycobacteria. It also suggests that these orthologs may have descended from a common ancestor and, therefore, that they can be viewed as orthologous members of the same protein family.

In mycobacteria, 6-d-Tal has been only described in GPLs so far. We next investigated the glycolipid profile, focusing on GPL from a set of slow-growing and rapidly-growing NTM clinical isolates, which are representative strains present in the phylogenetic tree (**Figure 6A**). TLC analysis of the apolar lipid fraction of all species from a broad panel showed an intense band around R_f 0.43 that was attributed to TDM **(Figure S7A)**. TLC analysis of polar lipids in chloroform/methanol/water (65:25:4, v/v/v) also showed phospho-*myo*-inositol mannosides (PIMs) in all species **(Figure S7B)**. Subsequent TLC analysis using chloroform/methanol/water (90:10:1, v/v/v) as solvent revealed a wider lipid diversity, including GPL-like compouds that were differentially expressed **(Figure 6B)**. Overall, of the fifteen strains tested, ten strains (marked +) showed bands corresponding to GPL, whereas five (marked –) did not. Some strains showed similar TLC patterns such as *M. avium* and *M. gilvum* or *M. genavense* and *M. lentiflavum*, suggesting that these pairs of strains have close GPL profiles. The other GPL-positive strains (*M. abscessus*, *M. aurum*, *M. goodii*, *M. simiae, M. moriokaense* and *M. paraffinicum*) showed distinct TLC patterns, indicating a large structural variability in their GPL content. As a control, we checked that the identified GPL-related compounds were still detected as lower R_f bands following saponification. In contrast, all bands disappeared in *M. branderi*, *M. chelonae*, *M. mageritense, M. malmoense* and *M. scrofulaceum* further confirming the absence of GPLs in these species **(Figure S8)**. We further established by GM/FID and GC/MS the monosaccharides composition of

the native polar lipid fractions from all the species in order to confirm the species-specific expression of GPLs (**Figure 6C**). All ten identified GPL-positive species expressed a wide range of deoxyhexose residues, including 6-d-Tal and its methylated-analogues (2-*O*-methyl 6-d-Tal, 3-*O*-methyl 6-d-Tal), and Rha with methylated analogues (3-*O*-methyl Rha, 3,4 di-*O*-methyl Rha, 2,3,4 tri-*O*-methyl Rha) in different ratios. The 6-d-Tal or its methylated forms were detected in all strains, whereas Rha or its methylated forms were detected in all strains except *M. paraffinicum* that exclusively expressed 6-d-Tal. The presence of 3-*O*-methyl 6-d-Tal in *M. genavense*, *M. lentiflavum*, *M. simiae* and *M. moriokaense* has already been observed in previous studies, in agreement with the present work. In contrast, the polar lipids of three of the five GPL-negative strains (*M. branderi, M. chelonae, M. mageritense*) did not show any traces of deoxyhexoses. Finally, *M. malmoense* and *M. scrofulaceum* showed low quantities of 6-d-Tal, Rha and 3-*O*-methyl Rha, suggesting that these two strains may synthetise deoxyhexose independently of GPL. Altogether, these results indicate the exlusive presence of 6-dTal in all GPL-like molecules in mycobacteria, albeit with traces found in *M. scrofulaceum*.

Deletion of *tle* in *M. abscessus* results in increased pathogenicity in zebrafish

M. abscessus S and R variants have very different infection outcomes when injected in zebrafish embryos (27, 30). While R leads to acute infection and high embryo mortality, S is less virulent and more associated with chronic persistent infection. Therefore, because we observed a R morphoptype upon knocking-out *tle*, we wanted to use the zebrafish model to evaluate the effect of this mutation on the infection outcome. To do so, 30 hpf embryos were infected with approximately 250 CFU of either R, S, Δ*tle*, Δ*tle::*C (all strains expressing a red fluorescent marker) or the PBS control, and monitored for embryo survival, bacterial burden and whole embryo imaging as outlined in **Figure 7A**. As expected, mortality of embryos injected with Δ*tle* was much higher than the S wild-type progenitor (10% and 42%, respectively) and more like the R morphotype (40%) at 12 dpi **(Figure 7B)**. Complementation was only partial, similar to what was observed *in vitro*, with 21% of embryo mortality. In agreement with the enhanced embryo mortality, bacterial burden was significantly higher in embryos infected with Δ*tle,* to levels close to the R strain, compared to S progenitor while infection with Δ*tle::*C led to bacterial loads comparable to those found with the S strain **(Figure 7C)**. These results were confirmed by embryo imaging, where we can clearly see very small infection foci in embryos injected with S and the

complemented strain at 3 dpi **(Figure 7D)**, while embryos injected with the mutant were similar to the R, with a higher number of infected foci as well as a bigger size.

DISCUSSION

6-deoxy-Talose is a rare deoxyhexose found in Gram-negative, Gram-positive bacteria and mycobacteria as a component of the cell wall and capsule structures (10, 35, 38, 42). The activated nucleotide sugar form of 6-d-Tal is dTDP-6-d-Tal, which is synthesised from Glc-1-phosphate and dTTP *via* the Rml pathway. Until now, the origin of the dTDP-6-d-Tal used by Gtf1 for talosylation of GPL remained unknown. Based on the structural predictions with validated epimerases and the development of an enzymatic assay, we demonstrate here that MAB_4111c/Tle catalyses the epimerisation of dTDP-Rha to dTDP-6-d-Tal, an activity lost when the catalytic Y181 or substrate-binding residues are replaced with alanine. Since the epimerization to TDP-6-d-Tal appears only partial *in vitro*, it is possible that *in vivo*, the activity of Tle is coupled with and/or regulated by the cognate glycosyltransferase Gtf1, previously shown to attach the talose residue to the GPL peptidic backbone (35).

Genomic analyses further showed that *tle* ortologues are widely distributed in actinomycetes, and was found in approximately 42% of all mycobacterial species for which a genome sequence is available (52). Even though GPL from various species appear structurally different, our compositional analysis indicates that all contain 6-d-Tal (or 2-*O*-methyl-6-d-Tal or 3-*O*-methyl-6-d-Tal) and that these species all possess a *tle* gene. Conversely, a few species failed to produce GPLs despite the presence of *tle*, although it is very likely that these strains (at least some of them) do not produce GPL due to the presence of mutation in the *gpl* biosynthetic and transport gene cluster, as demonstrated previously in *M. abscessus* (13). *M. avium* represents another typical example of an NTM producing GPL which encodes a *tle* gene. Interestingly, the lack of 6-d-Tal attached to the *allo*-threonine in a R variant of *M. avium* MAC 104 has been previously reported (53), and the genetic lesion responsible for the loss of 6-dTal in this strain corresponded with the deletion of a genomic region containing *gtfA*, an ortholog of *gtf1* (54). This further supports the hypothesis that the loss of 6-d-Tal conditioning a R morphotype is not specific to *M. abscessus* but can be extrapolated to other NTMs.

To validate the structure-function relationship between Tle and 6-d-Tal-containing GPL, we generated a *tle* unmarked deletion in the *M. abscessus* S variant. A thorough lipid analysis clearly emphasized the absence of 6-d-Tal in the GPL of the mutant strain, while the presence of Rha residues remained intact. Previously, we characterized a *gft1* mutant, which, similarly to the *tle* mutant, produced GPL lacking 6-d-Tal. Gtf1 uses dTDP-6-d-Tal produced by Tle, as a substrate to

glycosylate the D-*allo*-Thr residue of GPL. In addition to the loss of 6-d-Tal, both Δ*gtf1* and Δ*tle* share in common other phenotypes. First, deletion of *tle* produces a virtually R morphotype, although it appeared creamy on plates, while deletion of *gtf1* generated colonies with a R and dry texture. Whereas the vast majority of clinical isolates of the R morphotype have mutations in the biosynthetic genes *mps1*, *mps2*, or transporter genes *mmpL4a/mmpL4b/mmpS4* (15), GPL glycosylation can also lead to colony morphological changes (10). This study shows that enzymes involved in the production of nucleotide-activated sugars can also lead to these morphological changes. However, it remains to be established whether mutations in *tle* are responsible for the acquisition of an R morphotype occuring during infection in the host. Second, while GPL are present in the outermost mycobacterial layer (10), their presence/absence or modifications in their structures can profoundly alter the surface properties of *M. abscessus*. Sliding motility may play an important role in surface colonisation by mycobacteria in the environment and in the host (35). The *tle* mutant showed considerably reduced sliding motility. Previous studies between S and R strains underscored the correlation between low GPL production and enhanced hydrophobicity with virulence (2, 10). As expected for a R variant, we found that Δ*tle* was more hydrophobic than the parental S variant, as reported previously for the *gf1* mutant (35). Third, the development of biofilms appears crucial for *M. abscessus* infections (55, 56). The deletion of *tle* altered the biofilm development of *M. abscessus*. Although most of the measured parameters (number of bacteria, colony volume and density) indicated that the *tle* mutant behaved similarly to the R morphotype, its colony shape was significantly different from that of the S and R morphotypes, as the colony height of the *tle* mutant was greater and colony diameter was less wide than that of the reference R strain. This emphasizes the importance of 6-d-Tal for shaping *M. abscessus* colony-biofilms. Herein, we also took advantage of using the zebrafish model of infection as a reliable and manageable model for revealing and comparing the difference in virulence between the parental S and the Δ*tle* strains (27, 57). Our results are consistent with the previous findings obtained with Δ*gtf1* (35) and indicate that, in the presence of the sole innate immunity, the loss of 6-d-Tal in GPL translates into increased pathogenesis and lethal infection in zebrafish embryos.

Overall, this study also emphasizes the biosynthetic interconnection between the arabinogalactan and GPL pathways in *M. abscessus*, as depicted in **Figure 8**. The mycobacterial cell wall consists of a mycolic acid layer that is bound to peptidoglycan *via* the polysaccharide arabinogalactan. Arabinogalactan is covalently bound to the peptidoglycan *via* the α-L-

rhamnopyranosyl-(1→3)-α-D-*N*-acetyglucosaminosyl-1-phosphate unit (58). On the one hand, the donor dTDP-Rha, used by the rhamnosyltransferase WbbL to produce the rhamnosyl-containing linker unit (59), is synthesized by four enzymes (RmlA-D) beginning with dTPP and Glc-1-phosphate. TDP-Rha biosynthesis is essential for the growth of mycobacteria (60), prompting to the development of dTDP-Rha inhibitors for new tuberculosis therapeutics (61). On the other hand, the donor dTDP-Rha is also used by the rhamosyltransferases Gtf2 and Gtf3, which add the first and second Rha to the GPL biosynthetic intermediates. That dTDP-Rha stands on the crossroad between the arabinogalactan and GPL pathways is further substantiated by its direct use by Tle, which converts dTDP-Rha into dTDP-6-d-Tal, which is itself used by Gtf1 to talosylate the rhamnosylated GPL intermediates. However, while arabinogalactan (and disaccharide linker unit) is fundamental to the structural integrity of the cell wall and required for mycobacterial viability, this is not the case for the GPLs, which are lacking in the R strains of *M. abscessus*. However, the loss of GPL has important consequences on *M. abscessus* pathogenesis and infection outcome, as shown in various animal models (26, 27, 30, 35) and in humans (18, 24).

EXPERIMENTAL PROCEDURES

Mycobacterial strains, growth conditions, and reagents

M. abscessus CIP104536^T (S) and CIP104536^T (R) strains used in this study were previously sequenced and their genomic differences identified and characterized (13, 62). All bacterial strains and plasmids used for this study are listed in **Table S2** and **Table S3**, respectively. Mycobacteria were grown in Middlebrook 7H9 broth (BD, New Jersey, USA) supplemented with 0.025% tyloxapol and 10% oleic acid- albumin-dextrose-catalase enrichment (OADC) (7H9^{OADC}) or on Middlebrook 7H10 agar (BD) containing 10% OADC (7H10^{OADC}) at 37 °C, with antibiotics when required. A Bio-Rad Gene pulser (25 µF, 2500 V, 800 Ω) was used to transform electrocompetent mycobacteria. After transformation, strains carrying the pMV306 (48) derivatives were selected on 250 µg/mL kanamycin.

Expression of Tle in *E. coli*

MAB_4111c (tle) was PCR-amplified using *M. abscessus* genomic DNA using the specific primers (**Table S1**, primers 9-10) and Q5 polymerase. The amplicons were cloned into pET30 restricted with KpnI and EcoRI, enabling to introduce the genes in frame with the six-histidine tag. The resulting pET30-*tle* was used for site-directed mutagenesis of specific amino acids involved in the active site (Y181, primers 11-12) or the substrate-binding sites (S121, primers 13-14; N210, primers 15-16; R249, primers 17-18) using the QuikChange II Site-Directed Mutagenesis Kit (Agilent) and based on structural similarity with the *B. thailandensis* dTDP-L-Rha 4-epimerase (UniProt ID: Q2SYH7 · WBIB_BURTA). The pET30 constructs containing the native or mutated *tle* genes were used to transform *Escherichia coli* strain BL21 Star DE3 (Life Technologies). Cultures were grown in terrific broth medium containing 50 µg/mL kanamycin at 37 °C under agitation until an optical density at 600 nm (OD600) of 0.7-0.9 was achieved. Cultures were placed at 4 °C for 30 min before addition of 1 mM isopropyl β-D-1-thiogalactopyranoside (IPTG) and an overnight incubation at 16 °C under agitation. Bacteria were collected by centrifugation and pellets were resuspended in lysis buffer (50 mM Tris-HCl pH 8, 400 mM NaCl, 5% glycerol, supplemented with 10 mg/mL of NP-40, 78 µg/mL of dithiothreitol, 1 pill of cOmplete tablets, Mini EDTA-free, EASYpac per 50 mL, 2.175 mg/mL of imidazole and 1mg/mL of lysozyme) previously chilled on ice. Becteria were lysed by sonication and the lysate clarified by centrifugation (12,000 rpm at 4°C for 30 min), incubated overnight at 4 °C with nickel beads (Ni

Sepharose 6 Fast Flow, GE Healthcare), washed using washing buffer I (50 mM Tris-HCl pH 8, 350 mM NaCl, 5% glycerol, 78 µg/mL of dithiothreitol, 1 pill of cOmplete tablets, Mini EDTA-free, EASYpac per 50 mL, and 1.3 mg/mL of imidazole) and in washing buffer II (50 mM Tris-HCl pH 8, 200 mM NaCl, 5% glycerol, 78 µg/mL of dithiothreitol, 1 pill of cOmple tablets, Mini EDAT-free, EASYpac per 50 mL and 1.3 mg/mL of imidazole). Proteins were eluted in elution buffer (50 mM Tris pH=7, 100 mM NaCl, and 5% glycerol, and 17 mg/mL of imidazole) and then dialyzed overnight at 4 °C in dialysis buffer (50 mM Tris-HCl pH7, 200 mM NaCl, and 5% glycerol).

Enzymatic activity assay

A 50 µL reaction mixture (in 50 mM of PBS buffer pH 7.5) containing 10 mM of dTDP-L-Rha, 1 mM of $NADP^+$, and Nickel-beads eluted fractions enriched with the various MAB_4111c protein variants (0.42 µg/µL MAB_4111c, 0.31 µg/µL MAB_4111c-Y181A, 0.86 µg/µL MAB_4111c-S121A, 0.70 µg/µL MAB_4111c-N210A, 0.75 µg/µL MAB_4111c-R249A, and 0.69 µg/µL MAB_4111c-R249A/N210A/S121A) was incubated at 37 °C for 1 hr. The reaction was stopped by diluting the reaction with cooled buffer of acetonitrile/100 mM aqueous ammonium acetate pH 4.5 (60% acetonitrile). As a control reaction, a similar assay was performed by replacing dTDP-L-Rha by 10 mM of dTDP-D-Glc. The diluted solution was analyzed by HPLC equipped with UV detector at 254 nm using ZIC®-cHILIC column. The column was eluted at 40 °C with acetonitrile/100 mM aqueous ammonium acetate pH 4.5 (60% acetonitrile) at a flow rate of 0.6 mL/min. The enzyme activity was determined by the conversion of the product (Yield = [dTDP-6-deoxy-L-Tal]/([dTDP-6-deoxy-L-Tal] +[dTDP-L-Rha]). To analyse the activity by NMR, a reaction mixture consisting of 500 µL deuterium oxide(D_2O) containing 10 mg of dTDP-L-Rha, 5 mg of $NADP^+$, 5 mg of disodium hydrogen phosphate (Na_2HPO_4), and enriched MAB_4111c protein variants (0.14 µg/µL MAB_4111c, 0.13 µg/µL MAB_4111c-Y181A) was incubated at 37 °C for 5 hrs.

For the time-curve analysis, a 100 µL reaction mixture (in 50 mM of PBS buffer, pH 7.5) containing 10 mM of dTDP-L-Rha, 1 mM of $NADP^+$, and 0.42 µg/µL of MAB_4111c was incubated at 37 °C for different time point. The reaction was stopped by diluting the reaction with cooled buffer of acetonitrile/100 mM aqueous ammonium acetate pH 4.5 (60% acetonitrile). The diluted solution was analyzed by HPLC equipped with UV detector at 254 nm using ZIC®-cHILIC column. The column was eluted at 40 °C with acetonitrile/100 mM aqueous ammonium acetate pH 4.5 (60% acetonitrile) at a flow rate of 0.6 mL/min. All dTDP-activated sugar nucleotides were produced enzymatically, as reported previously (63).

LC-MS/MS analysis was performed on a triple quadrupole mass spectrometer LCMS8060XS (Shimadzu, Kyoto, Japan) coupled with a Nexcera system (Shimadzu, Kyoto, Japan). Chromatography was performed on a ZIC-cHILIC column as previously described (2.1 mm i.d. x 150 mm, 1.7 µm; SeQuant, Sweden) (64, 65). The mobile phases were: (A) 20 mM acetate buffer (pH 4.5) containing 90 % acetonitrile, and (B) the same buffer. The elution gradient was as follows: 12-18 % linear gradient of buffer B for 12 min; 18-25 % linear gradient of buffer B for 5 min; 25-55 % buffer B for 5 min; and 55 % buffer B for 5 min. The flow rate was maintained at 0.2 mL/min. Analysis of dTDP-rhamnose and dTDP-d-Tal was performed in the multiple reaction monitoring mode using the specific precursor ion $[M-H]^-$ at *m/z* 547.1 and product ion pairs at *m/z* 321.1. Product ion scanning was also conducted by MS/MS analysis of the precursor ion $[M-H]^-$ at *m/z* 547.1.

Structural modeling of Tle using AlphaFold 3

The dimeric structure of Tle was predicted using AlphaFold 3 (43). Two identical sequences of Tle, each comprising 353 amino acids, along with two copies of the NAD^+ ligand, were input into the AlphaFold 3 web server (https://alphafoldserver.com/). The server produced five model outputs. The model with the highest predicted local-distance difference test (pLDDT) score was selected for further analysis. The pLDDT score ranges from 0 to 100, where 0 indicates the lowest confidence and 100 the highest confidence in the structural prediction. Additionally, for multimeric targets, AlphaFold 3 provides predicted template modelling (pTM) and interface predicted template modelling (ipTM) scores, both ranging from 0 to 1, indicating the confidence in the predicted oligomeric state of the protein.

Deletion of *tle* and complementation in *M. abscessus*

The deletion mutant was generated in the S morphotype of the reference strain CIP104536^T (62) using the suicide vector pUX1-*katG* by double homologous recombination (47). Briefly, the upstream and downstream gene regions were PCR-amplified using the primers listed in **Table S1** and ligated into the PacI/NheI-linearized pUX1-*katG*. After transformation, bacteria were selected on 7H10^{OADC} supplemented with 250 µg/mL kanamycin with a visual screening of red fluorescent colonies, which have undergone the first homologous recombination. The second homologous recombination event was induced by isoniazid counter-selection and selected on 7H10^{OADC} with 50 µg/mL isoniazid and screening for non-fluorescent colonies and susceptibility

523 to kanamycin (35, 47). Complementation was performed by introducing a complementation
524 plasmid generated using the integrative pMV306 **(Table S3)**. Genes in fusion with a super folder
525 green fluorescent protein (sfGFP)-tagging sequence were amplified by PCR under the control of
526 the endogenous promoter. Proper gene deletion and all plasmids were verified by PCR and DNA
527 sequencing.
528
529 **Western blotting**
530 Fifty millilitres of cultures were grown in minimal salt medium (1 g/L KH_2PO_4, 500 mg/L NaCl, 2
531 g/L Na_2HPO_4, 1 g/L NH_4Cl, 200 µM $CaCl_2$, 2 mM $MgSO_4$, 5% glycerol, and 0.02% tyloxapol). The
532 bacterial pellet was washed twice with PBS supplemented with 0.025% tyloxapol (v/v) and
533 resuspended in PBS supplemented with cOmplete™ protease inhibitors cocktail (Roche, Sigma
534 Aldrich) and disrupted by bead beating using 1-mm diameter glass beads and a Mixer Mill MM
535 301 (Retsch, Germany) for two pulses of 3 min at 30 Hz. Protein concentration was determined
536 using the BCA Protein Assay Reagent kit (Thermo Fisher Scientific), according to the
537 manufacturer's instructions. Equal amounts of proteins (20 µg) were separated by 12% SDS-
538 PAGE, transferred onto a nitrocellulose membrane, probed for 1 hr with either mouse anti-GFP
539 (dilution 1:1000; Sigma) (antibodies-online GmbH, Aachen, Germany) or mouse anti-Antigen 85
540 (dilution 1:20; loading control) antibodies. Membranes were washed with PBS supplemented
541 with 0.02% Tween20 (w/v) and incubated for 45 min with goat anti-mouse antibody conjugated
542 to HRP (dilution 1:5000; Abcam). Bands were revealed using a SuperSignal West Femto
543 (ThermoFisher Scientific) and a ChemiDoc MP system (Bio-Rad laboratories). For detection of the
544 MAB_4111c variants produced in *E. coli*, the membrane was probed with anti-His mouse
545 monoclonal antibodies (dilution 1:1000) and incubacted with HRP-labeled goat anti-mouse
546 IgG(H+L) (dilution 1:2000).
547
548 **Growth, colony morphology, biofilm formation and sliding motility**
549 Growth curves were established based on cultures grown for 72 hrs and diluted in $7H9^{OADC}$ to
550 reach an initial OD_{595nm} of 0.05 and dispensed in flat-bottom 96-well microtiter plates (200 µL per
551 well). Plates were statically incubated at 37 °C and measurements were taken on a daily basis
552 using a spectrophotometer multimode microplate reader (Tecan Spark 10M, Tecan Group Ltd.,
553 Switzerland).

554 Colony morphology was assessed from 72 hrs cultures in 7H9^{OADC} and streaked on 7H10^{OADC}.
555 Plates were incubated at 37 °C for 5 days and photographed using a Zeiss microscope equipped
556 with a Zeiss Plan Neo Fluor Z13/0.25 FWD objective and an Axiocam503 monochrome camera
557 (Zeiss, Jena, Germany). Images were processed using ZEN 2 (Blue Edition).
558 *M. abscessus* biofilm formation was performed following a modification of the colony-biofilm
559 model previously described (66). Briefly, *M. abscessus* cultures were grown in Middlebrook
560 7H9^{OADC}, 0.2% glycerol and tyloxapol (0.025%) at 37 °C and 80 rpm for 72 hrs. Cultures were
561 centrifuged at 3,500 rpm for 5 min, washed two times with PBS and then diluted to an OD_{600nm}
562 of 0.5 (~1.5×10^8 CFU/mL). White black, polycarbonate membranes (diameter, 13 mm; pore size
563 0.2 µm, Whatman, Merck, Darmstadt, Germany) were placed on 7H10^{OADC} and inoculated with
564 10 µL of the bacterial suspension. The membrane-supported biofilms were statically incubated
565 for 5 days at 37 °C. Afterwards, the membrane-supported biofilms were imaged and processed
566 using a ZEISS Axio Zoom V16 binocular equipped with a lighting device (Zeiss HXP 200C Zeiss,
567 Germany at 7× zoom, detecting the grey level. On biofilm fluorescence pictures, a straight line
568 was drawn (covering all the diameter of the biofilm-colony) and grey-level intensity (GLI) of each
569 pixel as retrieved to draw GLI spectra using ZEN 2 software (Blue Edition). The colony volume was
570 calculated by using the half volume of an ellipsoid: Colony volume = $2/3\times\pi\times GLIM\times(CD/2)^2$, where
571 GLIM is the GLI maximum and CD is the colony diameter in pixels. After taking pictures, each
572 membrane-supported biofilm was processed for quantifying the number of CFU/membrane.
573 Colony-biofilm density was estimated as a coefficient resulting of CFU/membrane and the colony
574 volume.
575 Sliding motility of each strain was evaluated using a modified methodology previously described
576 (28). For each strain, 10 µl of 24 hrs cultures (OD_{600nm} = 0.9–1.0) were dropped in the centre of
577 well from a 6-well containing 7H9 broth with 0.3% agar and without adding any carbon source.
578 The sliding distance was evaluated and measured after incubation for 10 days at 37 °C under
579 humidified conditions. This experiment was performed by using three biological replicates and
580 two technical replicates.
581
582 **Hydrophobicity assay**
583 Mycobacterial surface hydrophobicity was determined following the methodologies developed
584 previously (49). Each strain was seeded on 7H9^{OADC} at 37 °C for 72 hrs, and then some colonies
585 were resuspended and sonicated in 5 mL of 0.9% NaCl in PYREX® 16 × 100 mm disposable round-

bottom threaded culture tubes (Corning) before measuring the OD_{595nm} (A_0) of 200 µL in triplicate was measured using spectrophotometer multimode microplate reader (Tecan Spark 10M). Subsequently, 2 mL of hexadecane (Sigma Aldrich) was added to glass tubes, and the mixtures were vortexed for 30 s. After phase separation (~20 min), the OD_{595nm} of 200 µL in triplicate was measured using a multimode microplate reader. Subsequently, the aqueous phase (A_1) was measured again and compared to the organic phase. The percentage of cell surface hydrophobicity (H) of each strain immersed in the organic hexadecane phase was calculated using the equation $H\ (\%) = [(A_0 - A_1)/A_0] \times 100$. This experiment was performed by using three biological replicates and three technical replicates.

Transmission electron microscopy

72-hrs cultures were washed with PBS, immersed overnight at 4 °C in PHEM buffer containing 2.5% glutaraldehyde (pH 7.4), rinsed in PHEM buffer and post-fixed in 0.5% osmium acid and 0.8% potassium ferricyanide trihydrate for 2 hrs at room temperature and in the dark. After washing twice with PHEM buffer, mycobacteria were dehydrated in a graded series of ethanol solutions (30-100%) and embedded in EmBed 812 using an Automated Microwave Tissue Processor for electron microscopy (Leica). Seventy nanometre sections were cut at different levels of each block/stem using a microtome (Leica-Reichert Ultracut E, Leica), counterstained in 70% ethanol with 1.5% uranyl acetate and lead citrate and observed using a Tecnai F20 TEM at 120KV.

Drug susceptibility testing

Antimicrobial susceptibility was tested using broth microdilution following the European Committee on Antimicrobial Susceptibility Testing (EUCAST) (67). For this purpose, 96-well RAPMYCOI Sensititre ™ titration plates (Thermo Fisher Scientific, Massachusetts, USA) were used following the manufacturer's recommendations.

Phylogenetic analysis of *tle* orthologous genes

Ortholog genes of *tle* in the genus *Mycobacterium* were found using BLASTp (68) against the NCBI non-redundant (nr) database by limiting the search to mycobacteria (taxid:85007) with a full bacterial scientific name registered and extending the maximum target sequences up to 1,000. In case of having more than one time the same mycobacterial species name, only the one with

618 the highest identity percentage was considered. All the proteins related to the Rml pathway were
619 excluded from the analysis. Orthologs of *tle* in other bacteria (non-mycobacteria) were found in
620 a manner similar to that described above but excluding the search to Mycobacteria (taxid:85007)
621 and limiting the maximum target sequences to 100. The Molecular Evolutionary Genetics Analysis
622 (MEGA) version 11 software (69) was used to generate a ClustalW multiple sequence alignment
623 of all the sequence and to construct Neighbour-Joining tree. The obtained tree was redrawn using
624 TreeViewer Version 2.1.0 (70) and coloured with Inkscape (71). To structurally validate the
625 findings from the phylogenetic tree, we analysed the presence of GPL and their glycosidic
626 composition in 14 clinical NTM isolates identified with Genotype Mycobacterium CM or AS (Hain
627 Lifescience, Nehren, Germany) from the Department of Clinical Microbiology of the University
628 Hospital Fundación Jiménez Díaz (Madrid, Spain).
629
630 **Lipid extraction and analysis**
631 Rapid-growing and slow-growing mycobacteria were grown on 7H10^{OADC} agar plates for 72 hrs
632 and 7H9^{OADC} broth for at least 14 days. After growing, pellets were collected and lyophilized, then
633 25 to 50 mg of bacterial pellets were subjected to apolar lipid extractions using petroleum ether
634 (72). GPL were extracted from the polar fraction using chloroform/methanol/0.3% NaCl (9/10/3,
635 v/v/v) and then with chloroform/methanol/0.3% NaCl (5:10:4, v/v/v). The combined solvent
636 extracts were mixed for 5 min with chloroform and 0.3% NaCl (1:1, v/v) and centrifuged at 3,000
637 *g* for 5 min to separate the lower organic phase from the aqueous phase. The upper aqueous
638 layer was discarded, and the lower organic phase was evaporated under a stream of nitrogen
639 and resuspended in chloroform/methanol (2:1, v/v) for TLC analysis or itol-acetates derivation.
640 *Thin-layer chromatography (TLC) analysis.* Beetween 50-150 µg of each extract were spotted
641 along 5 mm lane on Silica gel 60 F254 plates (Merck). GPL were separated at 4 °C using
642 chloroform/methanol/water (90:10:1, v/v/v). More polar lipids were separated using
643 chloroform/methanol/water (65:25:4, v/v/v). Glycolipids were revealed by spraying the plates
644 with orcinol in 20% sulfuric acid and charring.
645 *Glycolipids saponification.* Five hundred µg of the polar lipid fraction were dried under nitrogen.
646 Then, 1 mL of 0.1 M sodium hydroxide in chloroform/methanol (1:1, v/v) was added, and heated
647 overnight at 37 °C. One mL of butanol and 1 mL of water were added and the mixture vortexed
648 for 1 min. After centrifugation for 30 s, the upper butanolic phase was dried under a nitrogen
649 stream and dissolved in 300 µL of chloroform/methanol (2:1, v/v).

Itol-acetates derivation. After addition of 1 mL of 4 M TFA the sample was heated for 4 hrs at 100 °C, dried and desiccated overnight. The monosaccharides were reduced for 4 hrs at room temperature in 500 µL $NaBH_4$ 10 mg/mL in 2 M NH_4 and stopped with concentrated glacial acetic acid. Samples were dried at 55 °C under a nitrogen stream by co-distillation with methanol five times, dessicated overnight. Samples were peracetylated in 500 µL anhydride acetic for 4 hrs at 80 °C. The reaction products were washed five times with chloroform/water (1:1, v/v). The chloroform-rich phase was then filtered, dried, and dissolved in 500 µL chloroform. For GC-FID, 1 µL of itol-acetate derivatives was injected in splitless mode with an automatic sampler on a Solgel 1 MS 30 m × 0.25 mm × 0.25 µm capillary column with the following gradient temperature: 120 to 230 °C at 3 °C/min, then to 270 °C at 10 °C/min. Compounds were detected either with a flame ionization detector or a single quadrupole on a HP7820 or 5975N (Agilent Technologies). Previously determined retention times of differentially methylated Rha and unmodified 6-d-Tal were used for identification (33) while electronic impact mass spectrometry was used for methylated 6-d-Tal determination.

MALDI-TOF mass spectrometry. Before spotting 1 µL on the MALDI plate, 10 µL of 20 mg/mL dihydroxybenzoïc acid (DHB) in chloroform/methanol (1:2, v/v) were mixed with 5 µL of the sample extract in chloroform/methanol (2:1, v/v). MS positive and negative spectra were acquired on an Axima Resonance (Shimadzu, Kyoto, Japan) in reflectron mode.

Zebrafish maintenance

Zebrafish (*Danio rerio*) were kept and handled in compliance with the guidelines of the European Union for handling laboratory animals and approved by the Direction Sanitaire et Vétérinaire de l'Hérault for the ZEFIX-CRBM zebrafish facility (Montpellier) (registration number C-34-172-39). All experiments were approved by Le Ministère de l'Enseignement Supérieur et de la Recherche under the reference APAFIS#24406-2020022815234677 V3. Eggs were obtained by natural spawning, quickly bleached, and incubated at 28.5 °C in Petri dishes containing E3 medium (5 mM NaCl, 0.17 mM KCl, 0.33 mM $CaCl_2$, 0.33 mM $MgSO_4$). The transgenic reporter line Tg*(mpx:eGFP)*^{il14} (73) was used in this study.

Zebrafish infection

At 24 hrs post-fertilization (hpf), embryos were enzymatically dechorionated using 1mg/mL of pronase (stock of 5mg/mL diluted in E3) and placed in 60 mm Petri dishes containing E3 at 28.5

°C. Microinjection was performed as previously described (74). Embryos were injected in the caudal vein with ±250 CFU of either the R, S, SΔ*tle*, carrying the pMV306-mScarlet, SΔ*tle::C* carrying the pTEC27-tdTomato or the PBS control. Injected embryos were then rinsed twice and transferred individually in 48-well plates containing E3 and randomized for survival assays and CFU counts. Inoculum was checked by microinjecting a PBS drop and plating it on $7H10^{OADC}$. For survival assay, embryos were monitored every 24 hrs for 12 days, and marked as dead in the absence of a heartbeat. Bacterial burden was determined at 2dpi, 3dpi and 5dpi as following: embryos were individually manually disrupted with pellet pestles in 50 µL of PBS supplemented with 0.025% of tyloxapol. Lysates were sonicated for 30 s after adding 50 µL of PBS supplemented with 2% of Triton-X-100. Serial dilutions were plated on LB agar plates containing rifampicin (15 µg/mL) and kanamycin (250 µg/mL) and incubated for 4 days at 37 °C.

Zebrafish microscopy

For zebrafish imaging, embryos were anesthetized with 0.02% buffered MS222 and immobilized with 0.5% low melting agarose in a lateral position. Images were acquired with an EVOS™ M7000 Imaging System at 3dpi and 5dpi with the Olympus™ 2X Objective PlanApo 0.08 NA and the EVOS 10x Objective 0.3NA using the EVOS™ Light Cube, GFP 2.0. After imaging, embryos were rinsed and transferred back the 48-well plate with fresh E3. Image processing was done using ZEISS ZEN3.7 software.

Statistical analyses

All analyses were performed using R commander (75–76) and/or GraphPad Prism version 9.0.0 for Windows (GraphPad Software). The normality of data was evaluated using a Shapiro-Wilk test. Descriptive data are cited as median and interquartile range in case of non-normal distribution for each of the variables were calculated. A non-parametric Kruskal-Wallis test was used to compared more than three groups and a Wilcoxon test was used to compared two groups. Zebrafish survival assays are represented in Kaplan-Meier graphs and analysed with a Log rank test. For determination of bacterial counts, CFU were $\log_{10}$ transformed and the significance between multiple selected groups was determined using one-way ANOVA with Šidák's Multiple Comparisons test after validating the normality of the data.

DATA AVAILABILITY

All data are contained within the manuscript and the Supporting Information. The raw data can be share upon request.

SUPPORTING INFORMATION

This article contains supporting information.

ACKNOWLEDGMENTS

We are grateful to M. Plays, P. Richard, and C. Hamela for zebrafish husbandry; Pr J. Esteban from the Fundación Jiménez Diaz University Hospital (Madrid, Spain) for his generous gift of NTM clinical isolates; and Chantal Cazevieille (Intitut des Neurosciences de Montpellier, Montpellier, France) for her technical assistance during the TEM imaging. We are grateful to the PAGes-P3M core facility (PLBS US 41 - UAR 2014) for providing the scientific and technical environment conducive to achieving this work.

FUNDING

This project has been funded by the French National Research Agency grants 19-CE15-0012-01 (SUNLIVE) and 20-CE44-0019 (ILIome), by the Fondation pour la Recherche Médicale (Equipe FRM EQU202103012588) and by JSPS Core-to-Core Program No. JPJSCCA202000007.

CONFLICT OF INTEREST

The authors report there are no competing interests to declare.

REFERENCES

1. Lee, M.-R., Sheng, W.-H., Hung, C.-C., Yu, C.-J., Lee, L.-N., and Hsueh, P.-R. (2015) *Mycobacterium abscessus* complex infections in humans. *Emerg. Infect. Dis*. **21**, 1638–1646
2. Johansen, M. D., Herrmann, J.-L., and Kremer, L. (2020) Non-tuberculous mycobacteria and the rise of *Mycobacterium abscessus*. *Nat. Rev. Microbiol*. **18**, 392–407
3. Luthra, S., Rominski, A., and Sander, P. (2018) The role of antibiotic-target-modifying and antibiotic-modifying enzymes in *Mycobacterium abscessus* drug resistance. *Front. Microbiol.* **9**, 2179
4. Griffith, D. E. (2019) *Mycobacterium abscessus* and antibiotic resistance: Same as it ever was. *Clin. Infect. Dis*. **69**, 1687–1689
5. Galassi, L., Donato, R., Tortoli, E., Burrini, D., Santianni, D., and Dei, R. (2003) Nontuberculous mycobacteria in hospital water systems: application of HPLC for identification of environmental mycobacteria. *J. Water Health* **1**, 133–139

6. Ghosh, R., Das, S., Kela, H., De, A., Haldar, J., and Maiti, P. K. (2017) Biofilm colonization of *Mycobacterium abscessus* : New threat in hospital-acquired surgical site infection. *Indian J. Tuberc*. **64**, 178–182
7. Fennelly, K. P., Ojano-Dirain, C., Yang, Q., Liu, L., Lu, L., Progulske-Fox, A., Wang, G. P., Antonelli, P., and Schultz, G. (2016) Biofilm formation by *Mycobacterium abscessus* in a lung cavity. *Am. J. Respir. Crit. Care Med*. **193**, 692–693
8. Padilla, P., Ly, P., Dillard, R., Boukovalas, S., Zapata-Sirvent, R., and Phillips, L. G. (2018) Medical tourism and postoperative infections: A systematic literature review of causative organisms and empiric treatment. *Plast. Reconstr. Surg.* **142**, 1644–1651
9. Rüegg, E., Cheretakis, A., Modarressi, A., Harbarth, S., and Pittet-Cuénod, B. (2015) Multisite infection with *Mycobacterium abscessus* after replacement of breast implants and gluteal lipofilling. *Case Rep. Infect. Dis*. **2015**, 1–6
10. Gutiérrez, A. V., Viljoen, A., Ghigo, E., Herrmann, J.-L., and Kremer, L. (2018) Glycopeptidolipids, a double-edged sword of the *Mycobacterium abscessus* complex. *Front. Microbiol*. **9**, 1145
11. Howard, S. T., Rhoades, E., Recht, J., Pang, X., Alsup, A., Kolter, R., Lyons, C. R., and Byrd, T. F. (2006) Spontaneous reversion of *Mycobacterium abscessus* from a smooth to a rough morphotype is associated with reduced expression of glycopeptidolipid and reacquisition of an invasive phenotype. *Microbiology* **152**, 1581–1590
12. Medjahed, H., Gaillard, J.-L., and Reyrat, J.-M. (2010) *Mycobacterium abscessus*: a new player in the mycobacterial field. *Trends Microbiol.* **18**, 117–123
13. Pawlik, A., Garnier, G., Orgeur, M., Tong, P., Lohan, A., Le Chevalier, F., Sapriel, G., Roux, A.-L., Conlon, K., Honoré, N., Dillies, M.-A., Ma, L., Bouchier, C., Coppée, J.-Y., Gaillard, J.-L., Gordon, S. V., Loftus, B., Brosch, R., and Herrmann, J. L. (2013) Identification and characterization of the genetic changes responsible for the characteristic smooth-to-rough morphotype alterations of clinically persistent *Mycobacterium abscessus*. *Mol. Microbiol.* **90**, 612–629
14. Dedrick, R. M., Smith, B. E., Garlena, R. A., Russell, D. A., Aull, H. G., Mahalingam, V., Divens, A. M., Guerrero-Bustamante, C. A., Zack, K. M., Abad, L., Gauthier, C. H., Jacobs-Sera, D., and Hatfull, G. F. (2021) *Mycobacterium abscessus* strain morphotype determines phage susceptibility, the repertoire of therapeutically useful phages, and phage resistance. *mBio* **12**, e03431-20
15. Park, I. K., Hsu, A. P., Tettelin, H., Shallom, S. J., Drake, S. K., Ding, L., Wu, U.-I., Adamo, N., Prevots, D. R., Olivier, K. N., Holland, S. M., Sampaio, E. P., and Zelazny, A. M. (2015) Clonal diversification and changes in lipid traits and colony morphology in *Mycobacterium abscessus* clinical isolates. *J. Clin. Microbiol.* **53**, 3438–3447
16. Batt, S. M., Minnikin, D. E., and Besra, G. S. (2020) The thick waxy coat of mycobacteria, a protective layer against antibiotics and the host's immune system. *Biochem. J*. **477**, 1983–2006
17. Roux, A.-L., Viljoen, A., Bah, A., Simeone, R., Bernut, A., Laencina, L., Deramaudt, T., Rottman, M., Gaillard, J.-L., Majlessi, L., Brosch, R., Girard-Misguich, F., Vergne, I., De Chastellier, C., Kremer, L., and Herrmann, J.-L. (2016) The distinct fate of smooth and rough *Mycobacterium abscessus* variants inside macrophages. *Open Biol.* **6**, 160185
18. Catherinot, E., Roux, A.-L., Macheras, E., Hubert, D., Matmar, M., Dannhoffer, L., Chinet, T., Morand, P., Poyart, C., Heym, B., Rottman, M., Gaillard, J.-L., and Herrmann, J.-L. (2009) Acute respiratory failure involving an R variant of *Mycobacterium abscessus*. *J. Clin. Microbiol*. **47**, 271–274
19. Villeneuve, C., Etienne, G., Abadie, V., Montrozier, H., Bordier, C., Laval, F., Daffe, M., Maridonneau-Parini, I., and Astarie-Dequeker, C. (2003) Surface-exposed glycopeptidolipids of *Mycobacterium smegmatis* specifically inhibit the phagocytosis of mycobacteria by human macrophages. *J. Biol. Chem* **278**, 51291–51300
20. Recht, J., Martínez, A., Torello, S., and Kolter, R. (2000) Genetic analysis of sliding motility in *Mycobacterium smegmatis*. *J. Bacteriol*. **182**, 4348–4351
21. Barrow, W. W., Davis, T. L., Wright, E. L., Labrousse, V., Bachelet, M., and Rastogi, N. (1995) Immunomodulatory spectrum of lipids associated with Mycobacterium avium serovar 8. *Infect Immun*. **63**, 126–133

22. Etienne, G., Villeneuve, C., Billman-Jacobe, H., Astarie-Dequeker, C., Dupont, M.-A., and Daffé, M. (2002) The impact of the absence of glycopeptidolipids on the ultrastructure, cell surface and cell wall properties, and phagocytosis of *Mycobacterium smegmatis*. *Microbiology* **148**, 3089–3100
23. Cullen, A. R., Cannon, C. L., Mark, E. J., and Colin, A. A. (2000) *Mycobacterium abscessus* infection in cystic fibrosis. Colonization or infection? *Am. J. Respir. Crit. Care Med.* **161**, 641–645
24. Jönsson, B. E., Gilljam, M., Lindblad, A., Ridell, M., Wold, A. E., and Welinder-Olsson, C. (2007) Molecular epidemiology of *Mycobacterium abscessus*, with focus on cystic fibrosis. *J. Clin. Microbiol.* **45**, 1497–1504
25. Li, B., Ye, M., Zhao, L., Guo, Q., Chen, J., Xu, B., Zhan, M., Zhang, Y., Zhang, Z., and Chu, H. (2020) Glycopeptidolipid genotype correlates with the severity of *Mycobacterium abscessus* lung disease. *J. Infect. Dis*. **221**, S257–S262
26. Catherinot, E., Clarissou, J., Etienne, G., Ripoll, F., Emile, J.-F., Daffé, M., Perronne, C., Soudais, C., Gaillard, J.-L., and Rottman, M. (2007) Hypervirulence of a rough variant of the *Mycobacterium abscessus* type strain. *Infect. Immun.* **75**, 1055–1058
27. Bernut, A., Herrmann, J.-L., Kissa, K., Dubremetz, J.-F., Gaillard, J.-L., Lutfalla, G., and Kremer, L. (2014) *Mycobacterium abscessus* cording prevents phagocytosis and promotes abscess formation. *Proc. Natl. Acad. Sci. U.S.A.* **111**, E943-952
28. Bernut, A., Viljoen, A., Dupont, C., Sapriel, G., Blaise, M., Bouchier, C., Brosch, R., De Chastellier, C., Herrmann, J.-L., and Kremer, L. (2016) Insights into the smooth-to-rough transitioning in *Mycobacterium bolletii* unravels a functional Tyr residue conserved in all mycobacterial MmpL family members. *Mol. Microbiol*. **99**, 866–883
29. Kam, J. Y., Hortle, E., Krogman, E., Warner, S. E., Wright, K., Luo, K., Cheng, T., Manuneedhi Cholan, P., Kikuchi, K., Triccas, J. A., Britton, W. J., Johansen, M. D., Kremer, L., and Oehlers, S. H. (2022) Rough and smooth variants of *Mycobacterium abscessus* are differentially controlled by host immunity during chronic infection of adult zebrafish. *Nat. Commun*. **13**, 952
30. Bernut, A., Nguyen-Chi, M., Halloum, I., Herrmann, J.-L., Lutfalla, G., and Kremer, L. (2016) *Mycobacterium abscessus*-induced granuloma formation is strictly dependent on TNF signaling and neutrophil trafficking. *PLoS Pathog.* **12**, e1005986
31. Ripoll, F., Deshayes, C., Pasek, S., Laval, F., Beretti, J.-L., Biet, F., Risler, J.-L., Daffé, M., Etienne, G., Gaillard, J.-L., and Reyrat, J.-M. (2007) Genomics of glycopeptidolipid biosynthesis in *Mycobacterium abscessus* and *M. chelonae*. *BMC Genomics*. **8**, 114
32. Whang, J., Back, Y. W., Lee, K.-I., Fujiwara, N., Paik, S., Choi, C. H., Park, J.-K., and Kim, H.-J. (2017) *Mycobacterium abscessus* glycopeptidolipids inhibit macrophage apoptosis and bacterial spreading by targeting mitochondrial cyclophilin D. *Cell Death. Dis*. **8**, e3012–e3012
33. Daher, W., Leclercq, L.-D., Viljoen, A., Karam, J., Dufrêne, Y. F., Guérardel, Y., and Kremer, L. (2020) *O*-Methylation of the glycopeptidolipid acyl chain defines surface hydrophobicity of *Mycobacterium abscessus* and macrophage invasion. *ACS Infect. Dis*. **6**, 2756–2770
34. Illouz, M., Leclercq, L.-D., Dessenne, C., Hatfull, G., Daher, W., Kremer, L., and Guérardel, Y. (2023) Multiple *Mycobacterium abscessus O*-acetyltransferases influence glycopeptidolipid structure and colony morphotype. *J Biol Chem*. **299**, 104979
35. Daher, W., Leclercq, L.-D., Johansen, M. D., Hamela, C., Karam, J., Trivelli, X., Nigou, J., Guérardel, Y., and Kremer, L. (2022) Glycopeptidolipid glycosylation controls surface properties and pathogenicity in *Mycobacterium abscessus*. *Cell Chem. Biol.* **29**, 910-924.e7
36. Ma, Y., Pan, F., and McNeil, M. (2002) Formation of dTDP-rhamnose is essential for growth of mycobacteria. *J. Bacteriol*. **184**, 3392–3395
37. Pérez, E., Constant, P., Lemassu, A., Laval, F., Daffé, M., and Guilhot, C. (2004) Characterization of Three glycosyltransferases involved in the biosynthesis of the phenolic glycolipid antigens from the *Mycobacterium tuberculosis* complex. *J. Biol. Chem.* **279**, 42574–42583
38. Maki, M. (2003) Biosynthesis of 6-deoxyhexose glycans in bacteria. *Glycobiology*. **14**, 1R – 15
39. Nakano, Y., Suzuki, N., Yoshida, Y., Nezu, T., Yamashita, Y., and Koga, T. (2000) Thymidine diphosphate-6-deoxy-L-lyxo-4-hexulose reductase synthesizing dTDP-6-deoxy-L-talose from *Actinobacillus actinomycetemcomitans*. *J. Biol. Chem*. **275**, 6806–6812

40. Yoo, H.-G., Kwon, S.-Y., Karki, S., and Kwon, H.-J. (2011) A new route to dTDP-6-deoxy-L-talose and dTDP-L-rhamnose: dTDP-L-rhamnose 4-epimerase in *Burkholderia thailandensis*. *Bioorg. Med. Chem. Lett.* **21**, 3914–3917
41. Kapopoulou, A., Lew, J. M., and Cole, S. T. (2011) The MycoBrowser portal: A comprehensive and manually annotated resource for mycobacterial genomes. *Tuberculosis*. **91**, 8–13
42. Kenyon, J. J., Shashkov, A. S., Senchenkova, S. N., Shneider, M. M., Liu, B., Popova, A. V., Arbatsky, N. P., Miroshnikov, K. A., Wang, L., Knirel, Y. A., and Hall, R. M. (2017) *Acinetobacter baumannii* K11 and K83 capsular polysaccharides have the same 6-deoxy-L-talose-containing pentasaccharide K units but different linkages between the K units. *Int. J. Biol. Macromol*. **103**, 648–655
43. Abramson, J., Adler, J., Dunger, J., Evans, R., Green, T., Pritzel, A., Ronneberger, O., Willmore, L., Ballard, A. J., Bambrick, J., Bodenstein, S. W., Evans, D. A., Hung, C.-C., O'Neill, M., Reiman, D., Tunyasuvunakool, K., Wu, Z., Žemgulytė, A., Arvaniti, E., Beattie, C., Bertolli, O., Bridgland, A., Cherepanov, A., Congreve, M., Cowen-Rivers, A. I., Cowie, A., Figurnov, M., Fuchs, F. B., Gladman, H., Jain, R., Khan, Y. A., Low, C. M. R., Perlin, K., Potapenko, A., Savy, P., Singh, S., Stecula, A., Thillaisundaram, A., Tong, C., Yakneen, S., Zhong, E. D., Zielinski, M., Žídek, A., Bapst, V., Kohli, P., Jaderberg, M., Hassabis, D., and Jumper, J. M. (2024) Accurate structure prediction of biomolecular interactions with AlphaFold 3. *Nature*. **630**, 493–500
44. Jörnvall, H., Persson, B., Krook, M., Atrian, S., Gonzàlez-Duarte, R., Jeffery, J., and Ghosh, D. (1995) Short-chain dehydrogenases/reductases (SDR). *Biochemistry*. **34**, 6003–6013
45. Ishiyama, N., Creuzenet, C., Lam, J. S., and Berghuis, A. M. (2004) Crystal structure of WbpP, a genuine UDP-N-acetylglucosamine 4-epimerase from *Pseudomonas aeruginosa*: substrate specificity in UDP-hexose 4-epimerases. *J. Biol. Chem*. **279**, 22635–22642
46. Marmont, L. S., Whitfield, G. B., Pfoh, R., Williams, R. J., Randall, T. E., Ostaszewski, A., Razvi, E., Groves, R. A., Robinson, H., Nitz, M., Parsek, M. R., Lewis, I. A., Whitney, J. C., Harrison, J. J., and Howell, P. L. (2020) PelX is a UDP-N-acetylglucosamine C4-epimerase involved in Pel polysaccharide-dependent biofilm formation. *J. Biol. Chem*. **295**, 11949–11962
47. Richard, M., Gutiérrez, A. V., Viljoen, A., Rodriguez-Rincon, D., Roquet-Baneres, F., Blaise, M., Everall, I., Parkhill, J., Floto, R. A., and Kremer, L. (2019) Mutations in the MAB_2299c TetR regulator confer cross-resistance to clofazimine and bedaquiline in *Mycobacterium abscessus*. *Antimicrob. Agents Chemother.* **63,** e01316-18
48. Stover, C. K., de la Cruz, V. F., Fuerst, T. R., Burlein, J. E., Benson, L. A., Bennett, L. T., Bansal, G. P., Young, J. F., Lee, M. H., and Hatfull, G. F. (1991) New use of BCG for recombinant vaccines. *Nature*. **351**, 456–460
49. Jankute, M., Nataraj, V., Lee, O. Y.-C., Wu, H. H. T., Ridell, M., Garton, N. J., Barer, M. R., Minnikin, D. E., Bhatt, A., and Besra, G. S. (2017) The role of hydrophobicity in tuberculosis evolution and pathogenicity. *Sci Rep*. **7**, 1315
50. Chatterjee, D., and Khoo, K.-H. (2001) The surface glycopeptidolipids of mycobacteria: structures and biological properties. *Cell. Mol. Life Sci.* **58**, 2018–2042
51. Mederos, L. M., Valdivia, J. A., Sempere, M. A., and Valero-Guillén, P. L. (1998) Analysis of lipids reveals differences between '*Mycobacterium habana*' and *Mycobacterium simiae*. *Microbiology* **144**, 1181–1188
52. Armstrong, D. T., Eisemann, E., and Parrish, N. (2023) A brief update on mycobacterial taxonomy, 2020 to 2022. *J. Clin. Microbiol*. **61**, e00331-22
53. Torrelles, J. B., Ellis, D., Osborne, T., Hoefer, A., Orme, I. M., Chatterjee, D., Brennan, P. J., and Cooper, A. M. (2002) Characterization of virulence, colony morphotype and the glycopeptidolipid of *Mycobacterium avium* strain 104. *Tuberculosis* **82**, 293–300
54. Eckstein, T. M., Belisle, J. T., and Inamine, J. M. (2003) Proposed pathway for the biosynthesis of serovar-specific glycopeptidolipids in *Mycobacterium avium* serovar 2. *Microbiology* **149**, 2797–2807
55. López-Roa, P., Esteban, J., and Muñoz-Egea, M.-C. (2022) Updated review on the mechanisms of pathogenicity in *Mycobacterium abscessus*, a rapidly growing emerging pathogen. *Microorganisms* **11**, 90

56. Degiacomi, Sammartino, Chiarelli, Riabova, Makarov, and Pasca (2019) *Mycobacterium abscessus*, an emerging and worrisome pathogen among cystic fibrosis patients. *Int. J. Mol. Sci.* **20**, 5868
57. Johansen, M. D., Spaink, H. P., Oehlers, S. H., and Kremer, L. (2024) Modeling nontuberculous mycobacterial infections in zebrafish. *Trends Microbiol.* **32**, 663-677
58. McNeil, M., Daffe, M., and Brennan, P. J. (1990) Evidence for the nature of the link between the arabinogalactan and peptidoglycan of mycobacterial cell walls. *J. Biol. Chem*. **265**, 18200–18206
59. Mills, J. A., Motichka, K., Jucker, M., Wu, H. P., Uhlik, B. C., Stern, R. J., Scherman, M. S., Vissa, V. D., Pan, F., Kundu, M., Ma, Y. F., and McNeil, M. (2004) Inactivation of the mycobacterial rhamnosyltransferase, which is needed for the formation of the arabinogalactan-peptidoglycan linker, leads to irreversible loss of viability. *J. Biol. Chem.* **279**, 43540–43546
60. Li, W., Xin, Y., McNeil, M. R., and Ma, Y. (2006) *rmlB* and *rmlC* genes are essential for growth of mycobacteria. *Biochem. Biophys. Res. Comm.* **342**, 170–178
61. Ma, Y., Stern, R. J., Scherman, M. S., Vissa, V. D., Yan, W., Jones, V. C., Zhang, F., Franzblau, S. G., Lewis, W. H., and McNeil, M. R. (2001) Drug targeting *Mycobacterium tuberculosis* cell wall synthesis: genetics of dTDP-rhamnose synthetic enzymes and development of a microtiter plate-based screen for inhibitors of conversion of dTDP-glucose to dTDP-rhamnose. *Antimicrob. Agents Chemother*. **45**, 1407–1416
62. Ripoll, F., Pasek, S., Schenowitz, C., Dossat, C., Barbe, V., Rottman, M., Macheras, E., Heym, B., Herrmann, J.-L., Daffé, M., Brosch, R., Risler, J.-L., and Gaillard, J.-L. (2009) Non mycobacterial virulence genes in the genome of the emerging pathogen *Mycobacterium abscessus*. *PLoS ONE*. **4**, e5660
63. Wei, F., Yuan, R., Wen, Q., and Wen, L. (2023) Systematic enzymatic synthesis of dTDP-activated sugar nucleotides. *Angew. Chem. Int. Ed. Engl*. **62**, e202217894
64. Harada, Y., Nakajima, K., Li, S., Suzuki, T., and Taniguchi, N. (2021) Protocol for analyzing the biosynthesis and degradation of N-glycan precursors in mammalian cells. *STAR Protoc*. **2**, 100316
65. Ito, J., Herter, T., Baidoo, E. E. K., Lao, J., Vega-Sánchez, M. E., Michelle Smith-Moritz, A., Adams, P. D., Keasling, J. D., Usadel, B., Petzold, C. J., and Heazlewood, J. L. (2014) Analysis of plant nucleotide sugars by hydrophilic interaction liquid chromatography and tandem mass spectrometry. *Anal. Biochem*. **448**, 14–22
66. Aguilera-Correa, J. J., Boudehen, Y.-M., and Kremer, L. (2023) Characterization of *Mycobacterium abscessus* colony-biofilms based on bi-dimensional images. *Antimicrob. Agents Chemother*. **67**, e0040223
67. Fröberg, G., Maurer, F. P., Chryssanthou, E., Fernström, L., Benmansour, H., Boarbi, S., Mengshoel, A. T., Keller, P. M., Viveiros, M., Machado, D., Fitzgibbon, M. M., Mok, S., Werngren, J., Cirillo, D. M., Alcaide, F., Hyyryläinen, H.-L., Aubry, A., Andres, S., Nadarajan, D., Svensson, E., Turnidge, J., Giske, C. G., Kahlmeter, G., Cambau, E., Van Ingen, J., and Schön, T. (2023) Towards clinical breakpoints for non-tuberculous mycobacteria - Determination of epidemiological cut off values for the *Mycobacterium avium* complex and *Mycobacterium abscessus* using broth microdilution. *Clin. Microbiol. Infect.* **29**, 758–764
68. Altschul, S. (1997) Gapped BLAST and PSI-BLAST: a new generation of protein database search programs. *Nucleic Acids Res.* **25**, 3389–3402
69. Tamura, K., Stecher, G., and Kumar, S. (2021) MEGA11: Molecular evolutionary genetics analysis Version 11. *Mol. Biol. Evol.* **38**, 3022–3027
70. Bianchini, G., and Sánchez-Baracaldo, P. (2024) TreeViewer: Flexible, modular software to visualise and manipulate phylogenetic trees. *Ecol. Evol*. **14**, e10873
71. Developers, I. W. Draw Freely, Inkscape. https://inkscape.org/
72. Besra, G. S. (1998) Preparation of cell-wall fractions from mycobacteria. *Methods Mol. Biol*. **101**, 91–107
73. Renshaw, S. A., Loynes, C. A., Trushell, D. M. I., Elworthy, S., Ingham, P. W., and Whyte, M. K. B. (2006) A transgenic zebrafish model of neutrophilic inflammation. *Blood*. **108**, 3976–3978

954 74. Boudehen, Y.-M., Tasrini, Y., Aguilera-Correa, J. J., Alcaraz, M., and Kremer, L. (2023) Silencing
955 essential gene expression in *Mycobacterium abscessus* during infection. *Microbiol. Spectr*. **11**,
956 e0283623.
957 75. Using the R Commander, https://socialsciences.mcmaster.ca/jfox/Books/RCommander/
958 76. Fox, J. (2005) The R Commander: A Basic-Statistics Graphical User Interface to R. *J. Stat. Softw.* **14**,
959 1–42

960 **FIGURE LEGENDS**

961

962 **Figure 1. MAB_4111c belongs to the GPL biosynthetic cluster and is a predicted epimerase. (A)**
963 Structure of diglycosylated (GPL-2a) and triglycosylated (GPL-3) glycopeptidolipids. The green,
964 blue and yellow shadings represent the lipid, peptide and glycosydic moieties of the GPL. Di-*O*-
965 acetyl 6-d-Tal is drawn in red. **(B)** *M. abscessus GPL* locus encoding enzymes involved in the
966 synthesis, modification, and transport of GPL. *MAB_4111c* is indicated in bold. **(C)** Alignment of
967 the protein sequence of dTDP-L-Rha 4-epimerase from the *B. thailandensis* (ATCC 700388)
968 (wbiB_BURTA) with that of MAB_4111c from *M. abscessus*. The orange and blue shadings
969 represent the non-conserved and conserved and amino acids, respectively. The red, green and
970 blue asterisks indicate residues involved in the putative NADH-binding site, the substrate-binding
971 site and the catalytic residue reported in *B. thailandensis*, respectively.

972

973 **Figure 2. Enzymatic activity of MAB_4111c. (A)** Reaction catalyzed by MAB_4111c. **(B) Upper**
974 **panel:** HPLC profile of the standards and products formed during the enzymatic reaction in the
975 presence of MAB_4111c or MAB_4111c_Y181A with dTDP-Rha and $NADP^+$. The incubation was
976 performed for 60 min. The product of the reaction is labeled with a red box. **Lower panel:** HPLC
977 profile of standard dTDP-Glc, standard dTDP-6-d-Tal and dTDP-Glc and $NADP^+$ incubated with
978 MAB_4111c for 60 min. **(C) Upper panel:** LC/MS profile of the enzymatic reaction mixture in
979 MRM mode using the specific precursor ion $[M-H]^-$ at *m/z* 547.1. **Lower panel:** MS^2 fragmentation
980 spectra of standard dTDP-6-d-Tal and the enzymatic reaction product (*). **(D)** ^1H NMR spectra of
981 dTDP-L-Rha and $NADP^+$; MAB_4111c with dTDP-L-Rha and $NADP^+$ after 120 min;
982 MAB_4111c_Y181A with dTDP-L-Rha and $NADP^+$ after 120 min; dTDP-6-d-Tal. The characteristic
983 peaks of dTDP-6-d-Tal are indicated with red arrows. **(E)** Kinetic analysis of the reaction catalyzed
984 by MAB_4111c in the presence of dTDP-L-Rha and $NADP^+$.

985

986 **Figure 3. Structural Prediction of Tle. (A)** Cartoon representation of the Alphafold 3 predicted
987 dimeric structure of Tle. The structure is colored according to the plDTT score range (blue=high
988 confidence, cyan=confidence, yellow=low confidence, orange=very low confidence). **(B) Left**
989 **panel:** cartoon representation of the predicted Tle homodimer, with each chain colored in green
990 and cyan. NAD is depicted as a stick model. **Right panel:** Alignment of the monomeric structure
991 of Tle with the WbpP crystal structure (Tle in cyan and WbpP in magenta).

992 **Figure 4. Deletion of *tle* in *M. abscessus* alters colony morphology, hydrophobicity, sliding**
993 **motility and biofilm-colony development. (A)** Knock-out of *tle* is associated with a switch from
994 a S to a R-like morphotype. The scale bar represents 1 mm. **(B)** The deletion of *tle* is associated
995 with a higher growth rate. The experiment was performed using two biological replicates with
996 six technical replicates per biological replicate. Deletion of *tle* modifies hydrophobicity **(C)** and
997 the sliding motility **(D-E)**. The hydrophobicity experiment was performed using three biological
998 replicates with three technical replicates per biological replicate. The sliding motility experiment
999 was performed using three biological replicates with two technical replicates per biological
1000 replicate. The black scale bar indicates 5 mm. **(F)** Representative 2- and 2.5-dimensional pictures
1001 of colony-biofilms on biofilm-supporting membranes after 5 days of incubation. The absence of
1002 *tle* alters the biofilm-colony growth **(F)** (the scale bar represents 2 mm) and the biofilm-colony
1003 profile **(G)** (green, dark grey, red and blue dots represent the profiles of S, R, Δ*tle* and Δ*tle*::C,
1004 respectively). The CFUs per membrane are shown in **(H)**, the colony volume in **(I)**, and the colony
1005 density in **(J)**. This experiment was performed using five biological replicates. The error bar
1006 denotes the interquartile range. *: $p<0.05$, **: $p<0.01$; and ***: $p<0.001$.
1007
1008 **Figure 5. Structural analysis of the GPL content in Δ*tle.* (A)** TLC analysis representative from
1009 three independent experiments of native apolar (left) and polar (right) lipid extracts. Lipids were
1010 separated using chloroform/methanol/water (90:10:1, v/v/v) followed by spraying with orcinol
1011 and charring. GPL-1b and GPL-2b previously described (35) from Δ*tle* display a lower R_f than wild-
1012 type GPL-2a and GPL-3, which are restored in Δ*tle::*C. TDM: trehalose dimycolate; DAT: Di-*O*-acyl
1013 trehalose. **(B)** TLC analysis of native (NaOH -) and saponified (NaOH +) polar fractions. Lipids were
1014 separated using chloroform/methanol/water (90:10:1, v/v/v) followed by spraying with orcinol
1015 and charring. The R_f of GPL-2a and GPL-3 from Δ*tle* are not modified as it is the case for S and
1016 Δ*tle::*C. **(C)** MALDI-TOF positive spectra of native polar lipid fraction (black, NaOH -) from the S
1017 and Δ*tle::*C strains show ions for GPL-2a at *m/z* 1257.9/1285.9 and for GPL-3 at *m/z* 1403.9/1432.
1018 Spectra from saponified polar lipid fraction (red, NaOH +) show a 84 u.m.a decrease, to
1019 1173.4/1201.4 and 1319.3/1347.4, corresponding to deacetylated dGPL-2a and dGPL-3, as
1020 previously described (34). Conversely, ions for GPL-1b at *m/z* 1013.8/1041.8 and from GPL-2b at
1021 1187.9 were intense in native and saponified polar extracts from Δ*tle.* **(D)** Relative proportion of
1022 each monosaccharides was determined in the GPL-enriched saponified polar lipid fraction. 6-d-
1023 Tal could only be detected in S and Δ*tle::*C.

Figure 6. Distribution of *tle* orthologues in NTM and correlation with the presence of 6-d-Tal. **(A)** Phylogenetic tree reconstructed using already available *tle* sequences. Non-mycobacterial species and mycobacterial species are represented in pink and blue areas, respectively. Green, yellow and red dots label slowly-growing, intermediately-growing and rapid-growing mycobacteria, respectively. **(B)** TLC analysis of the polar lipid fraction of a selected panel of NTM clinical strains, representative from two independent experiments. Lipids were separated using chloroform/methanol/water (90:10:1, v/v/v) followed by spraying with orcinol and charring. +: presence of GPL-like components, confirmed by their detection after saponification **(Figure S8)**. -: absence of GPL-like components. **(C)** Deoxyhexoses composition analysis of polar lipid fractions separated with GC and GC-MS. Relative area of identified monosaccharides (n=4) show Rha residues in green and 6-d-Tal in blue. Identification of 6-d-Tal and Rha was confirmed by the retention time and fragmentation pattern of standards while *O*-methylated Rha was determined previously (33, 35). Identification of 2- and 3-*O*-methyl 6-d-Tal was deduced from the retention time and fragmentation pattern. Relative areas of Rha and 6-d-Tal and their methylated forms are expressed as ratios of total monosaccharides.

Figure 7. Increased virulence and pathogenesis of Δ*tle* in a zebrafish embryo model of infection. **(A)** Schematic overview of *in vivo* experiments. **(B)** Survival of infected embryos with the R strain (275±27 CFU), the S strain (280±36 CFU), Δ*tle* (264±33 CFU) and Δ*tle::*C (281±47 CFU). The graph shows the result of 4 pooled independent experiments. Embryos were marked dead in the absence of a heartbeat. Statistical analysis was performed using Log-rank (Mantel-Cox) test. ****: $p<0.0001$; **: $p<0.01$, ns: non-significant. **(C)** Bacterial burden from infected embryos at 2, 3 and 5dpi. The graph shows the result of 3 pooled independent experiments. n=5 embryos per time-point per condition. CFU counts were Log10 transformed. Statistical analysis was performed per time point using ordinary one-way ANOVA with Šídák's multiple comparisons test, after verifying the normality of the data. *: $p<0.05$; **: $p<0.01$; ***: $p<0.001$ ****: $p<0.0001$. **(D)** Imaging of infected embryos at 3dpi. One zoomed representative image of the head is shown per condition. Scale bar, 0.2 mm.

Figure 8. The biosynthetic interconnections between the arabinogalactan and glycopeptidolipid pathways in *M. abscessus*. dTDP-L-Rha is generated by the successive action of the Rml pathway enzymes, consisting of RmlA (MAB_4113), RmlB (MAB_3779), RmlC

(MAB_3780) and RmlD (MAB_3613c). This dTDP-L-Rha is used by WbbL (MAB_3612c) to produce the Rha-N-acetyl-glucosaminyl-phosphate disccharide unit that cross-links arabinogalactan to peptidoglycan. In addition, dTDP-L-Rha is also used by Gtf2 (MAB_4104) and Gtf3 (MAB_4112c) for GPL rhamnosylation (blue arrows). dTDP-6-d-Tal, produced from dTDP-L-Rha by the dTDP-Rha-4-epimerase (MAB_4111c/Tle) serves as the substrate for the talosyltransferase Gtf1 (green arrows), which adds one 6-d-Tal unit to mono- or di-rhamnosylated GPL precursors. The glycosylated GPLs (GPL-2a and GPL-3) are then transported across the inner membrane by the MmpL4 complex (MAB_4116c, MAB_4115c, MAB_4117c) and inserted into the outer leaflet of the mycomembrane in the *M. abscessus* S variant.

Figure 1

A

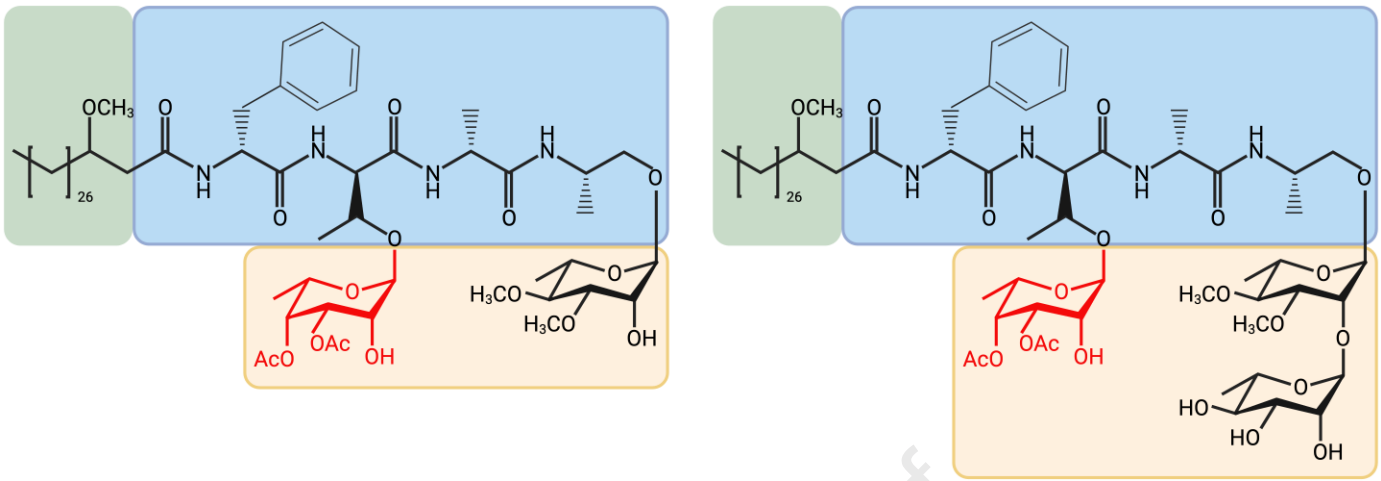

B

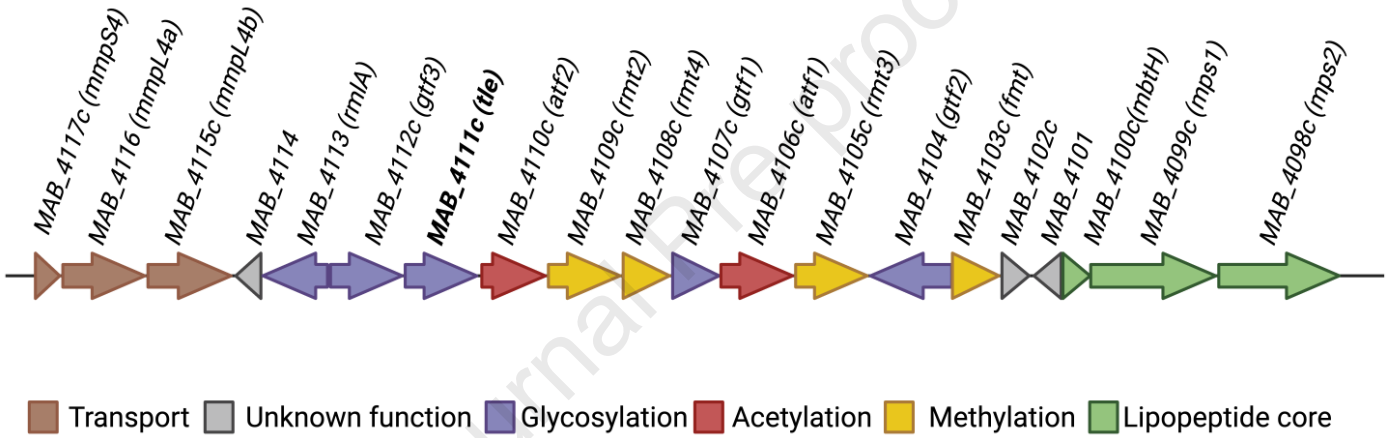

C

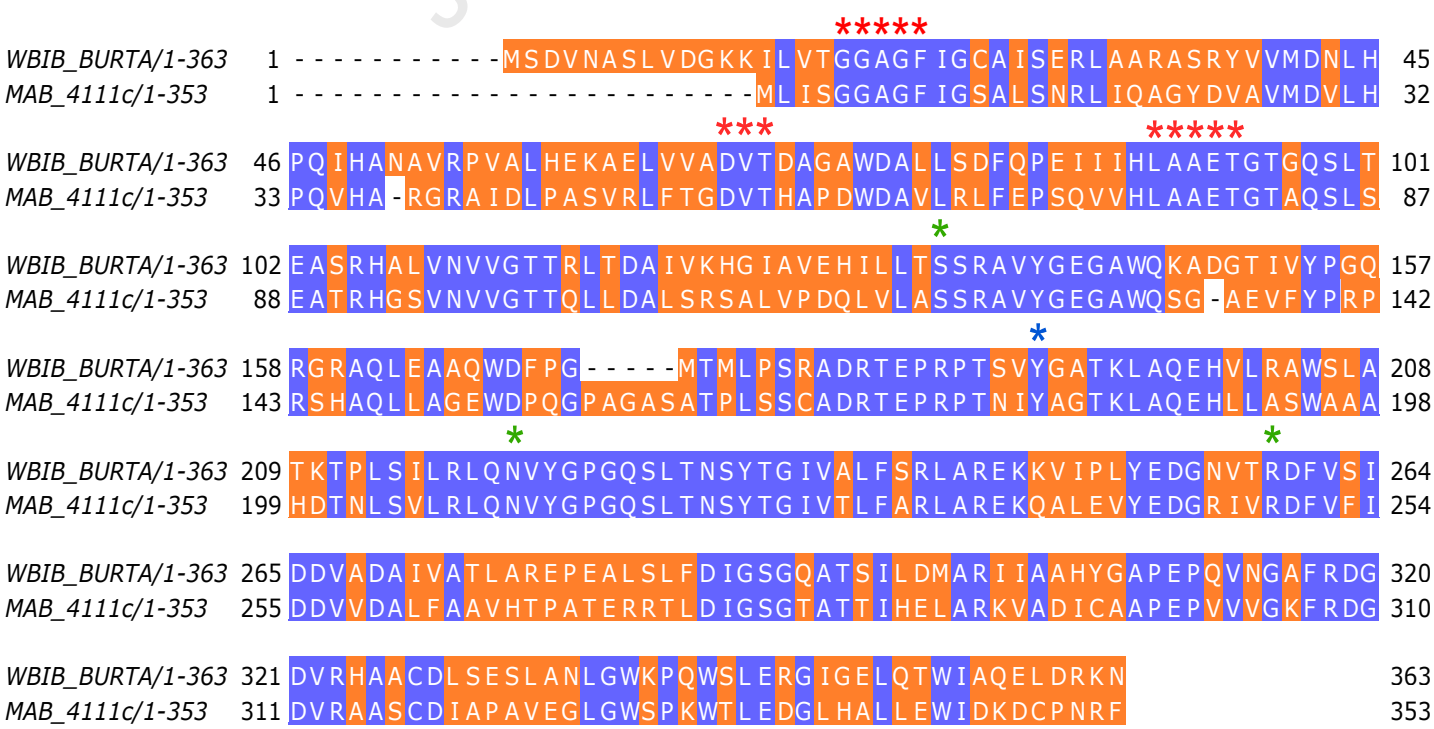

Figure 2

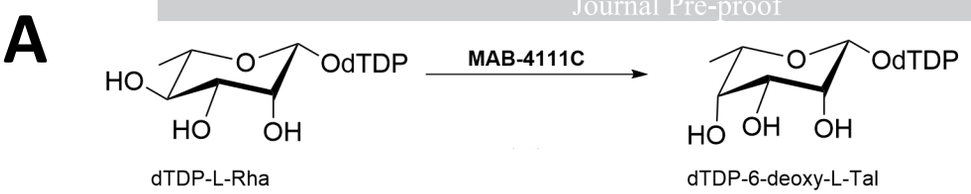

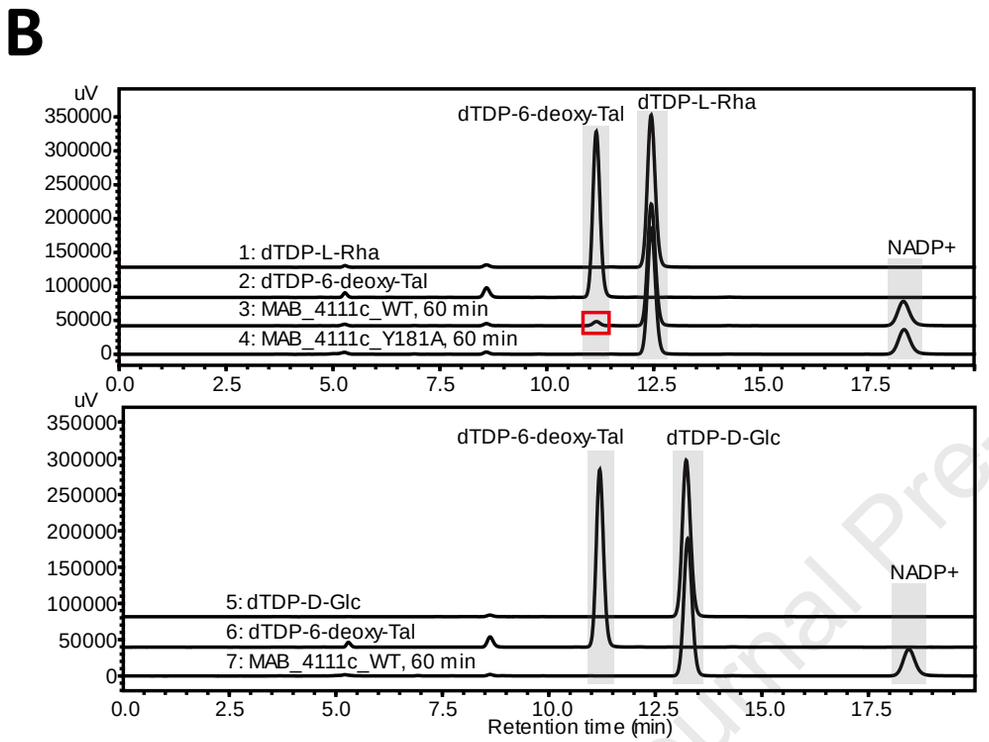

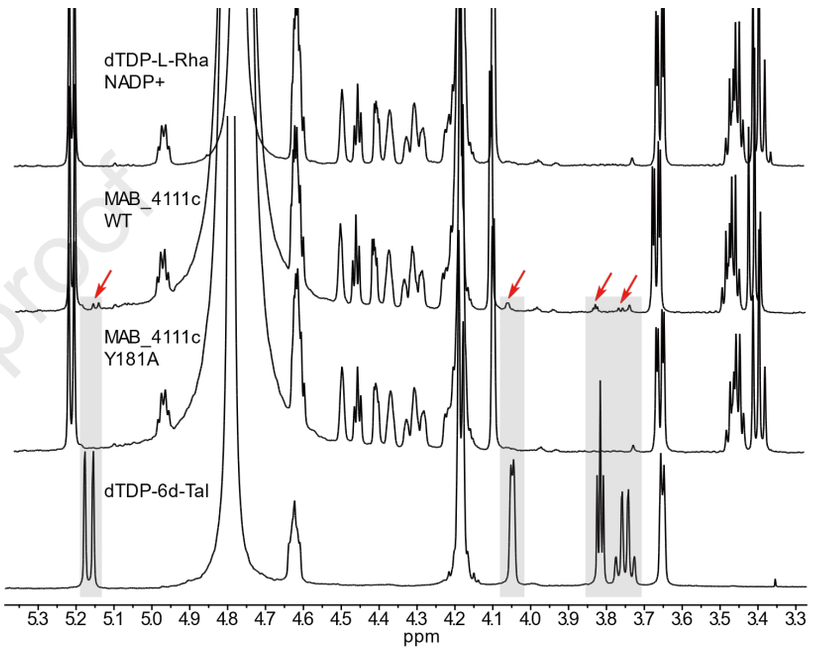

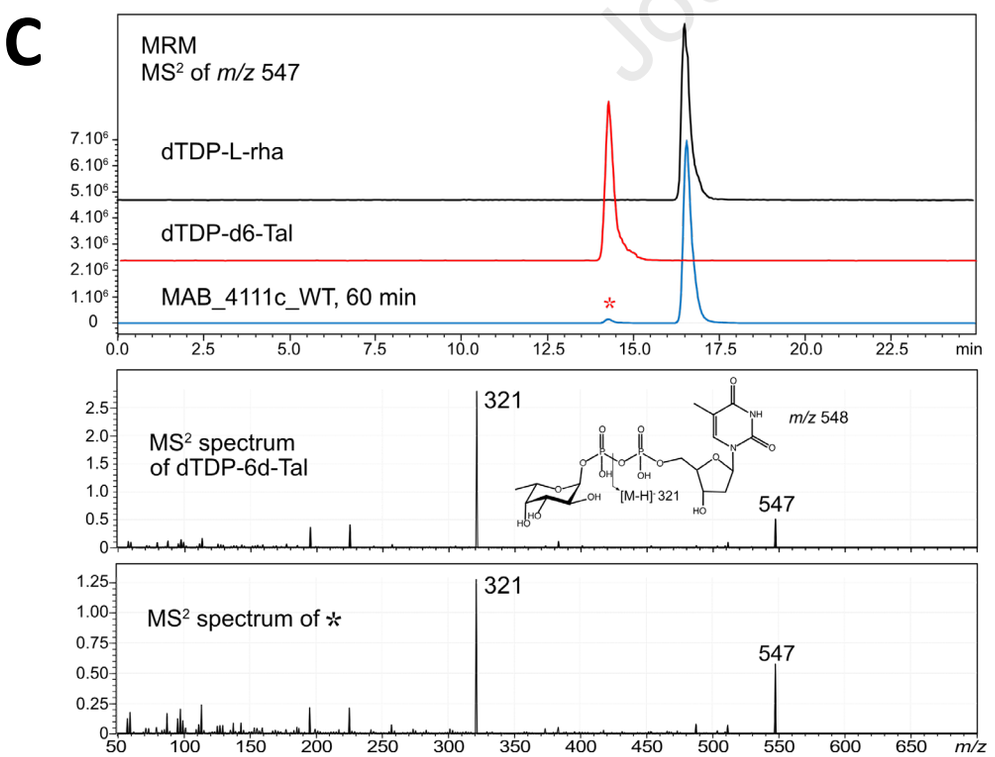

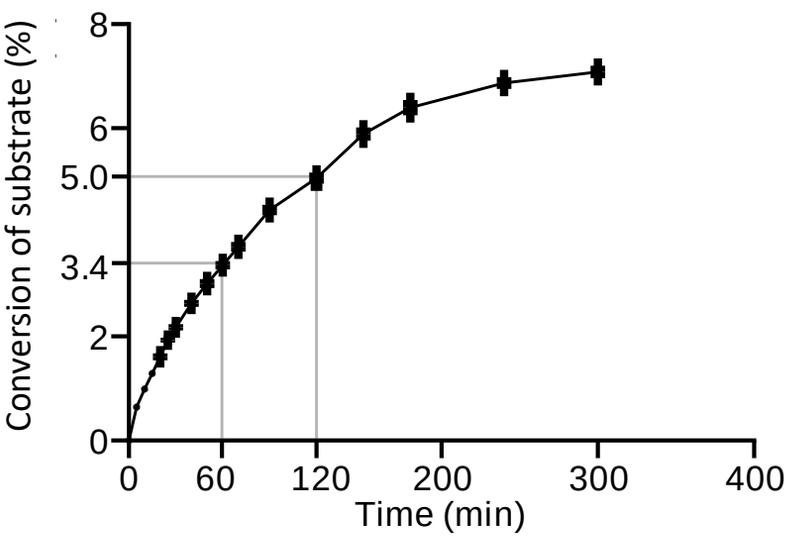

Figure 3

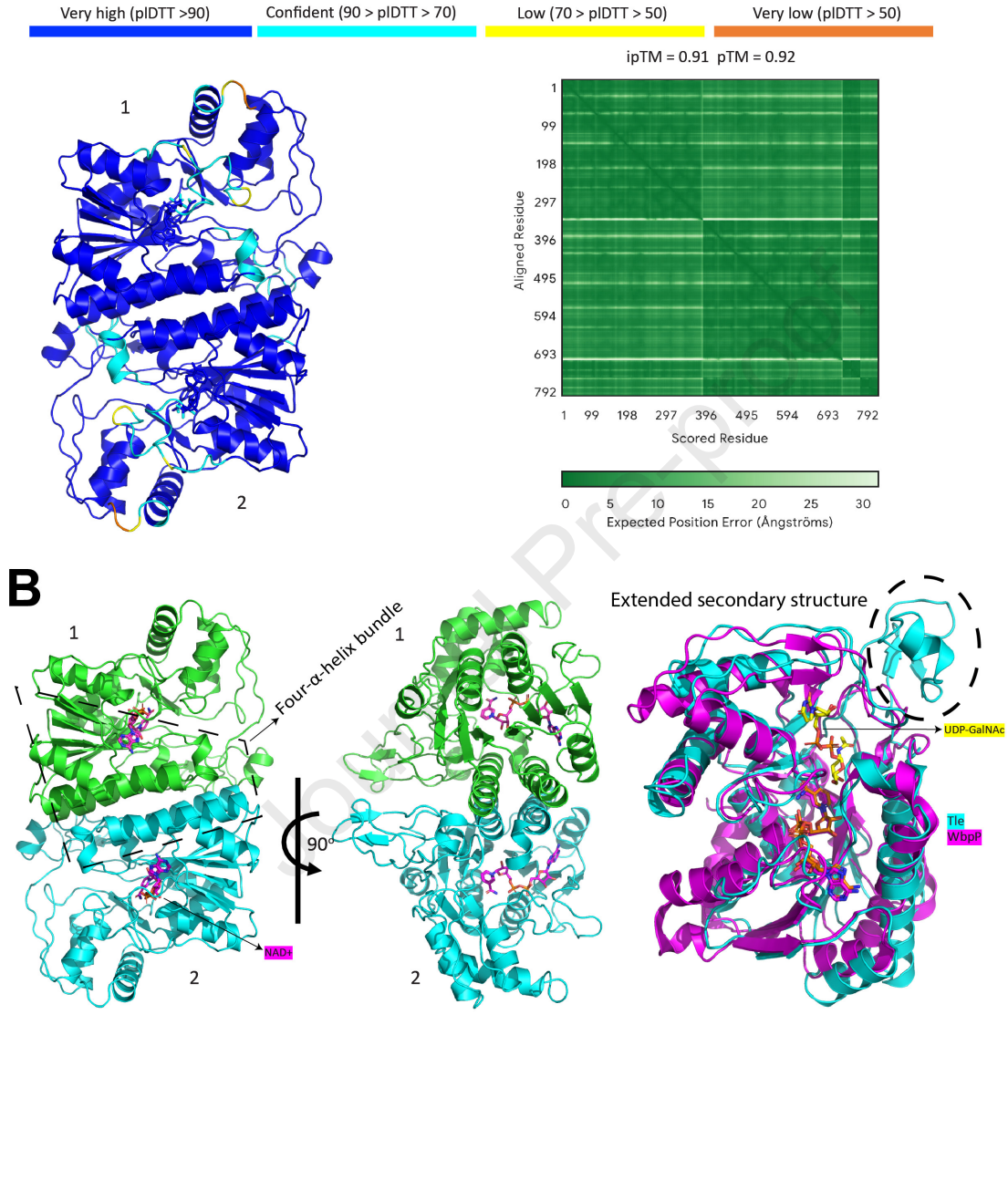

! "

Figure 4

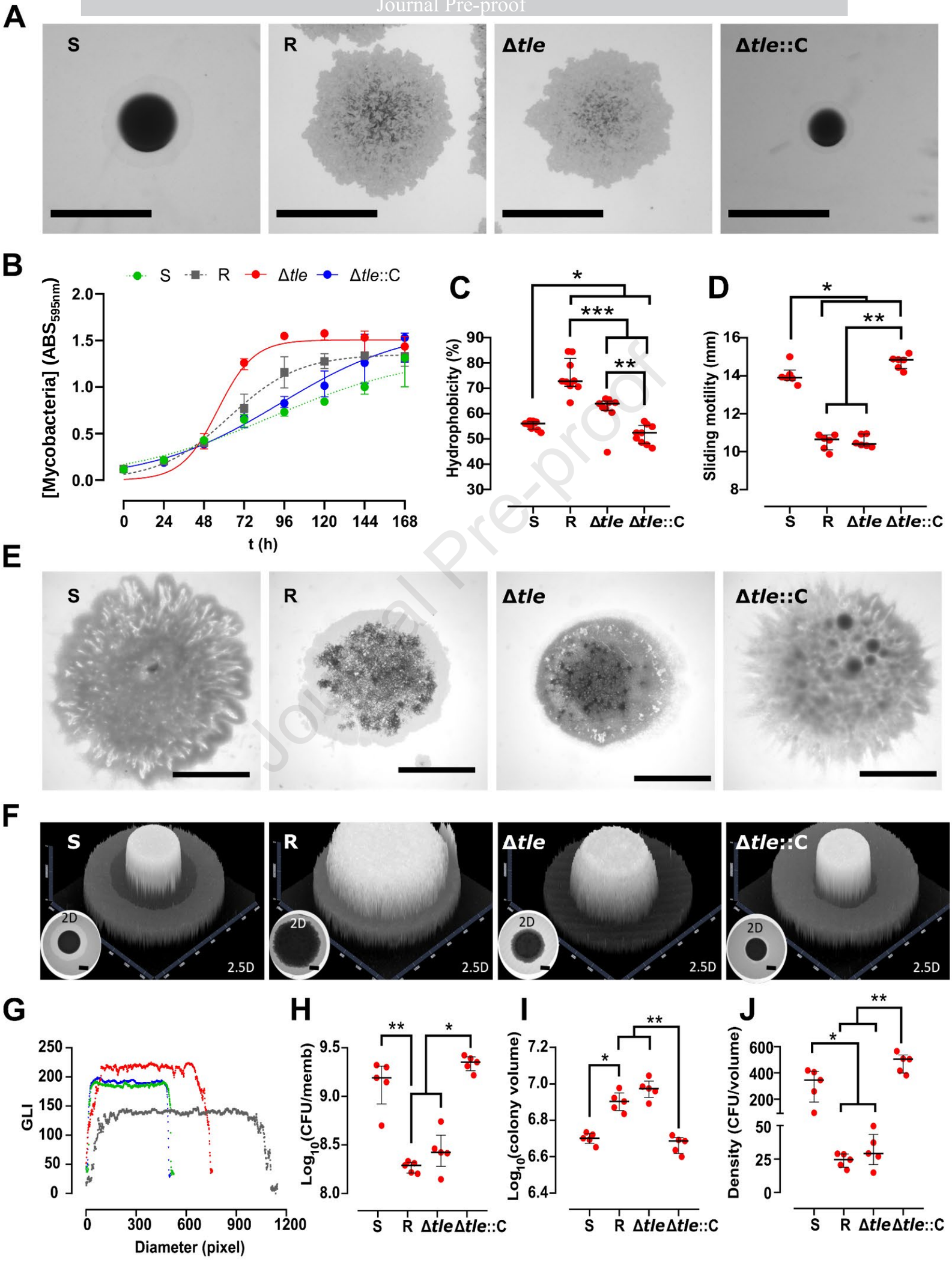

Figure 5

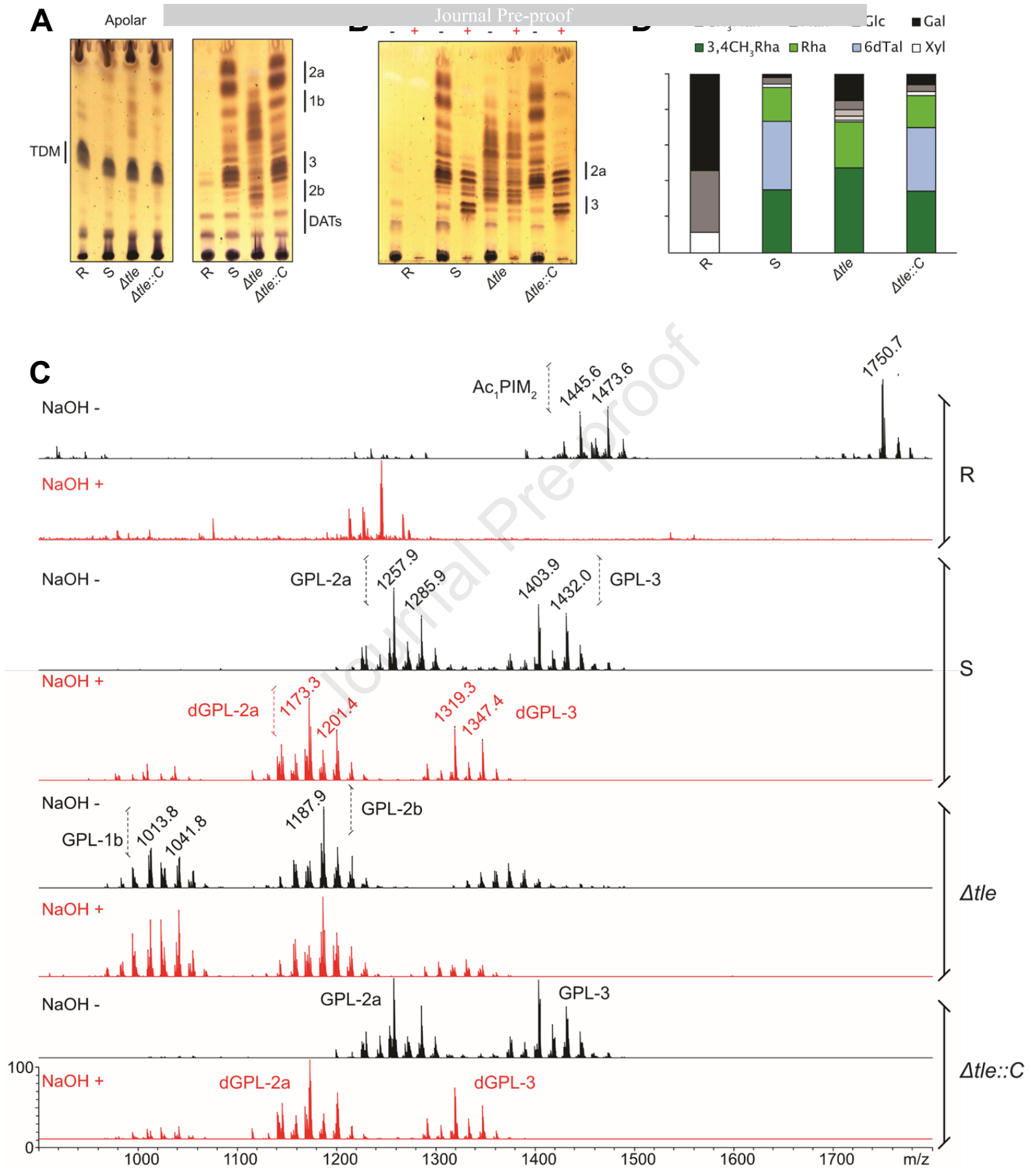

Figure 6

A

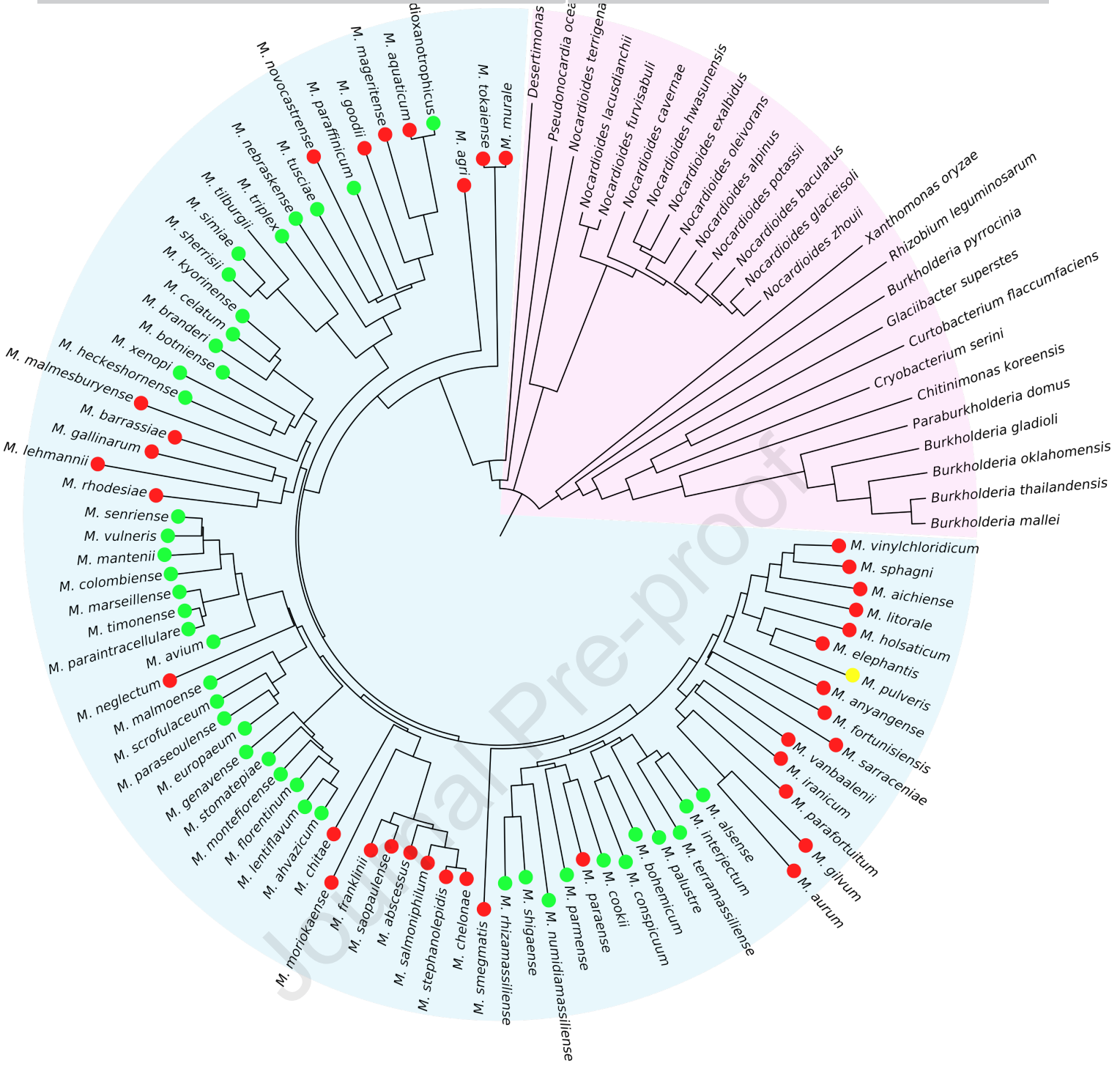

B

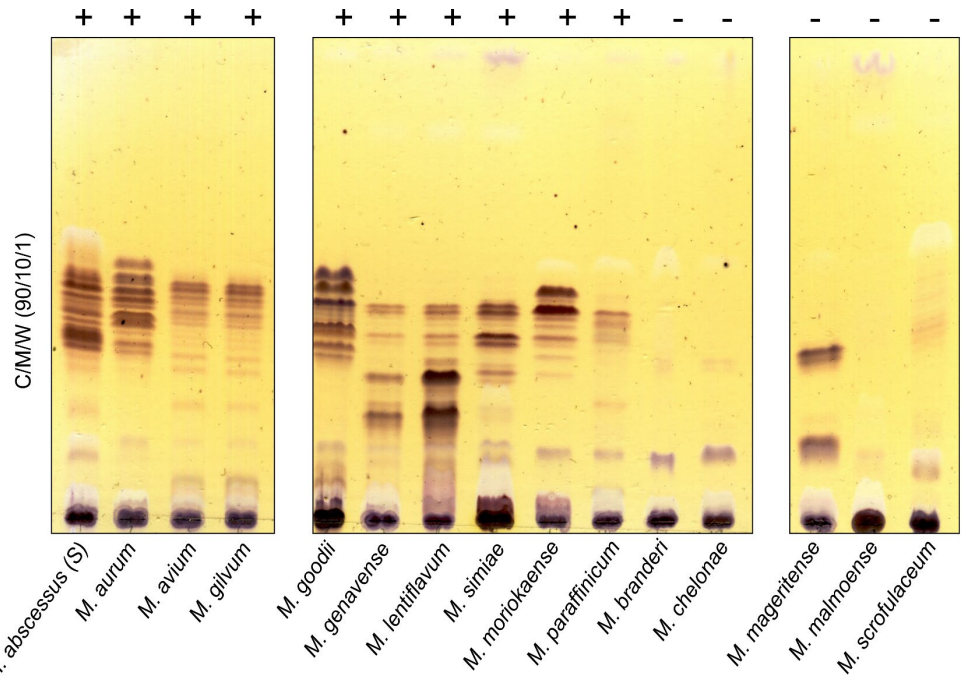

C

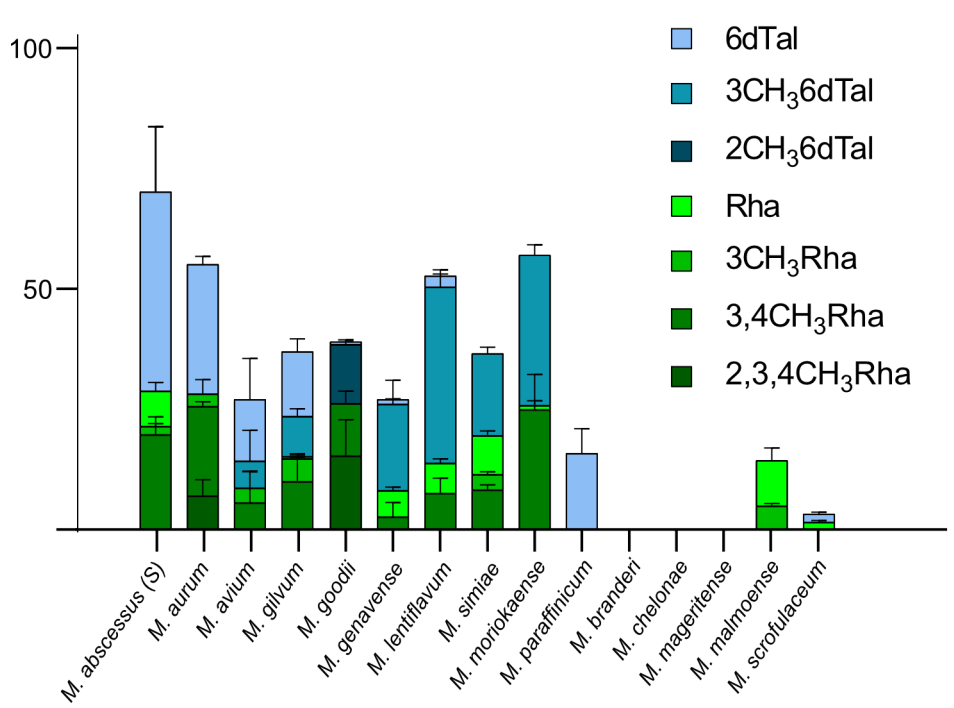

Figure 7

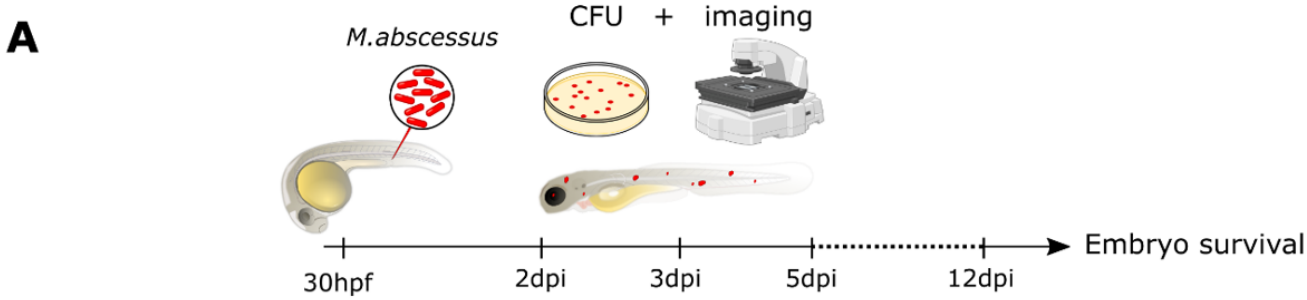

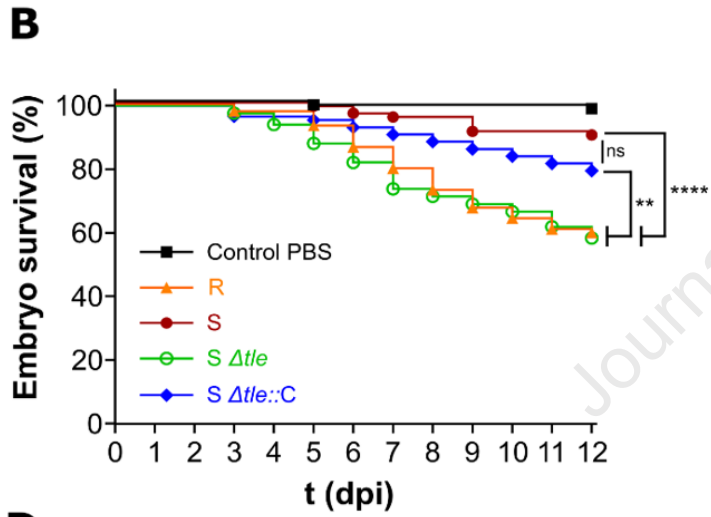

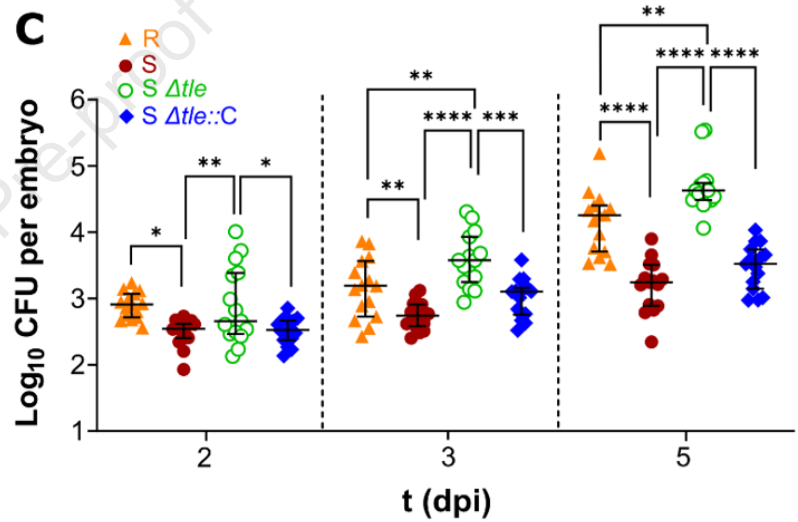

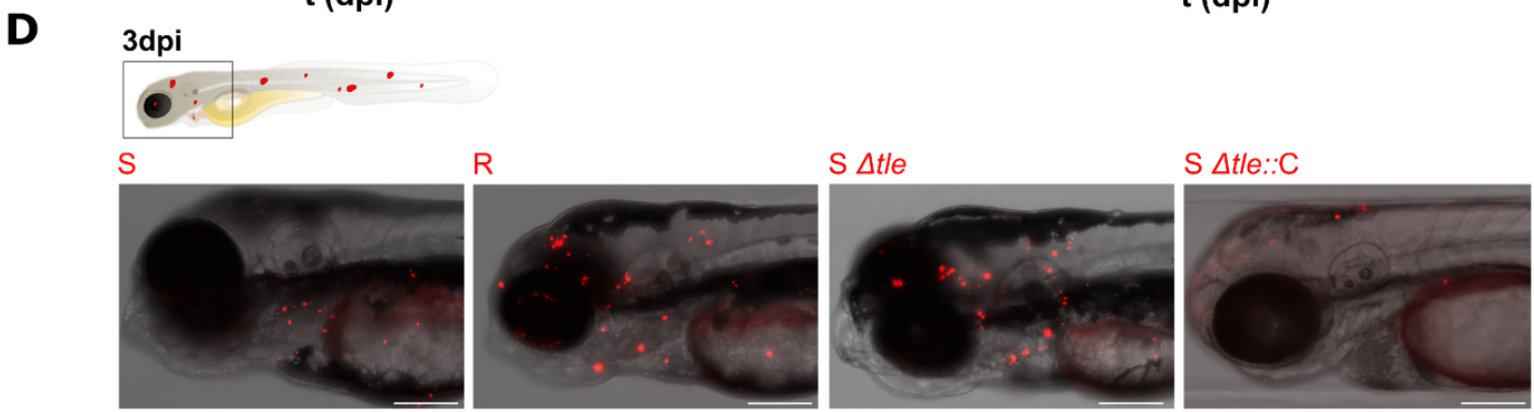

Figure 8

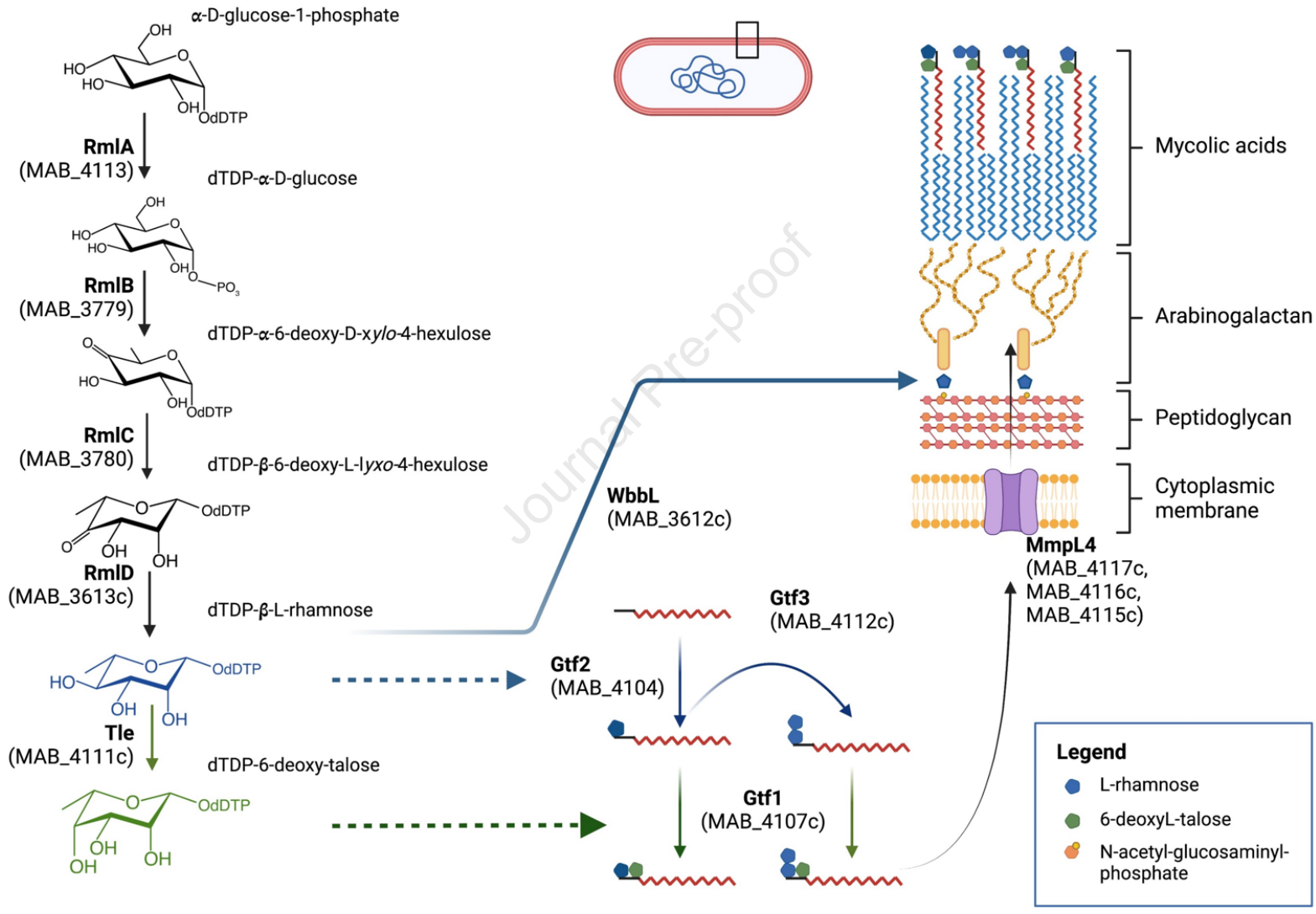

Declaration of interests

☒ The authors declare that they have no known competing financial interests or personal relationships that could have appeared to influence the work reported in this paper.

☒ The author is an Editorial Board Member/Editor-in-Chief/Associate Editor/Guest Editor for *[Journal name]* and was not involved in the editorial review or the decision to publish this article.

☐ The authors declare the following financial interests/personal relationships which may be considered as potential competing interests: